

Review

# Recent Trends and Advances of Silicon-Based Integrated Microwave Photonics

Reza Maram <sup>1</sup>, Saket Kaushal <sup>2</sup>, José Azaña <sup>2</sup> and Lawrence R Chen <sup>1,\*</sup>

<sup>1</sup> Department of Electrical and Computer Engineering, McGill University, Montreal, QC H3A 0E9, Canada; reza.maramqartavol@mcgill.ca

<sup>2</sup> Department of Energy, Materials and Telecommunications (EMT), Institut National de la Recherche Scientifique (INRS), Montreal, QC H5A 1K6, Canada; kaushal.saket@gmail.com (S.K.); azana@emt.inrs.ca (J.A.)

\* Correspondence: lawrence.chen@mcgill.ca; Tel.: +1-514-398-1879

Received: 23 December 2018; Accepted: 28 January 2019; Published: 30 January 2019



**Abstract:** Multitude applications of photonic devices and technologies for the generation and manipulation of arbitrary and random microwave waveforms, at unprecedented processing speeds, have been proposed in the literature over the past three decades. This class of photonic applications for microwave engineering is known as microwave photonics (MWP). The vast capabilities of MWP have allowed the realization of key functionalities which are either highly complex or simply not possible in the microwave domain alone. Recently, this growing field has adopted the integrated photonics technologies to develop microwave photonic systems with enhanced robustness as well as with a significant reduction of size, cost, weight, and power consumption. In particular, silicon photonics technology is of great interest for this aim as it offers outstanding possibilities for integration of highly-complex active and passive photonic devices, permitting monolithic integration of MWP with high-speed silicon electronics. In this article, we present a review of recent work on MWP functions developed on the silicon platform. We particularly focus on newly reported designs for signal modulation, arbitrary waveform generation, filtering, true-time delay, phase shifting, beam steering, and frequency measurement.

**Keywords:** microwave photonics; integrated optics; photonic integrated circuit; silicon photonics; optical generation and processing of microwave signals; photonic microwave filters; true-time delay; beam steering; frequency measurement; phase shifting

## 1. Introduction

Microwave photonics (MWP) is a multidisciplinary research discipline which bridges the photonics and microwave engineering worlds and investigates the handling of analog microwave signals using photonic devices and technologies for microwave applications, most prominently in telecommunications and sensing systems (the term microwave is used freely throughout the literature to designate either RF, microwave, or millimeter-wave signals) [1–9]. This emerging field has driven growing interest over the last three decades, mostly after the groundbreaking realization of the potential of optical links for the transmission of microwave signals in the 1990s [10–12]. Following these pioneering results, extensive research has been directed toward MWP [3,4,6,8,9,13–19], especially on solutions for the generation, transmission, and processing of microwave signals, because of its enormous potential for new technological applications in telecommunications [7]. In particular, at the present time, MWP provides new ways and possibilities to approach the emerging information technology scenarios, such as 5G mobile communications and Internet of Things (IoT), with capabilities beyond those of conventional electronic systems, in terms of enhanced flexibility,

scalability, and capacity [1,6–8,20,21]. The massive bandwidth, electromagnetic interference immunity, and flexible photonic platform are intrinsic remarkable advantages of MWP solutions to efficiently generate, transmit over low-loss optical fibers, and process microwave signals, overcoming inherent electronic limitations [2–4,8,20,22]. Figure 1 shows the schematic of a generic MWP system consisting of three main blocks: (1) a transmitter, (2) a MWP processor, and (3) a receiver. Various photonic components have been employed in these blocks, including optical sources (continuous wave (CW) and pulsed lasers), optical amplifiers, dispersive elements, electro-optic modulators, optical filters, and photodetectors (PDs). In many MWP systems, the transmitter consists of a CW/pulsed laser and optical phase/intensity modulator, with the radio-frequency (RF) signal being applied as the drive voltage to the modulator (in arbitrary waveform generation applications, the input signal is typically a short optical pulse). The modulated optical signal is then launched to a MWP processor, in which it is suitably manipulated through photonic devices. Examples of realized MWP functionalities include microwave photonic filters (MPFs) [23–25], arbitrary waveform generation (AWG) [14,26,27], beam steering [28–30], and phase shifting [31–34]. The manipulated optical signal is finally converted back to the microwave domain in the receiver, which typically consists of a photodiode.

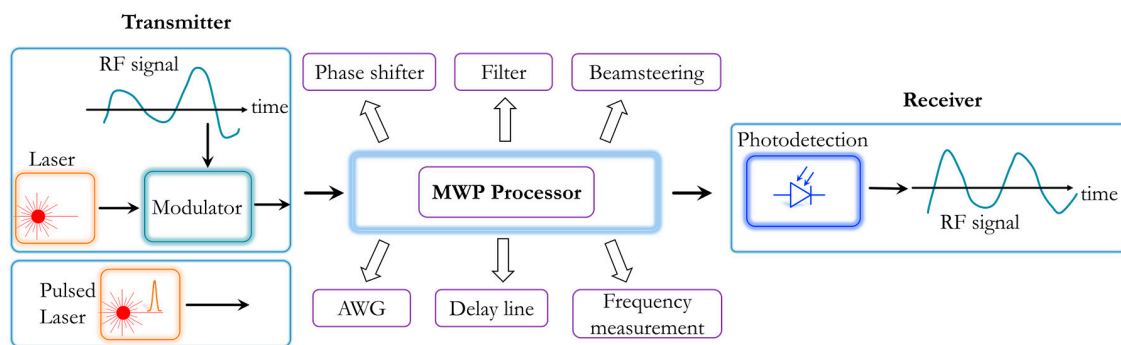


**Figure 1.** Architecture of a generic microwave photonic system. AWG: arbitrary waveform generation; MWP: microwave photonics; RF: radio-frequency.

MWP systems have relied almost exclusively on discrete photonic devices, fiber-based components, and standard optical fibers [7,18,23,35]. However, these configurations are bulky, power consuming, lossy, expensive, and lack the desired flexibility and stability [3,7,36]. Therefore, since 2005, there has been a strong drive for miniaturizing MWP systems onto a single chip to handle analog signals with low power, high efficiency, and high reliability metrics, which can be additionally reconfigured via software-defined networking (SDN) techniques [3,7,36–39]. As such, integrated photonics technologies have been increasingly adopted by the MWP community to implement MWP functionalities [7,20,40–43]. This has led to a second generation of MWP platforms termed ‘Integrated Microwave Photonics’ (IMWP). The roadmap towards experimental demonstration of IMWP functionalities has involved the use of different technology platforms [3,44], such as Indium Phosphide (InP) [21,45–47], Silicon-on-Insulator (SOI), which is the mainstay of silicon photonics [40,41,48–51], Silicon Nitride (Si<sub>3</sub>N<sub>4</sub>) [52–55], and Chalcogenide glass [56–58]. Each technology has specific sets of strengths and weaknesses [3]. Compared with other platforms, however, silicon technology offers critical practical advantages, such as low cost, small footprint, and good tunability (in terms of tuning speed and tuning range using thermo-optic or electro-optic effects) [22,40,59,60]. Another intrinsic advantage of silicon technology is that decades of advances in silicon circuit fabrication have resulted in well characterized, automated processes [51,59,60]. Packaging technology has followed in step. SOI-integrated optical fabrication is offered now at several foundries at very low cost. The resulting SOI chips can be mounted in standard packages surrounded by commercial silicon CMOS electronics and optical fiber communication. Hence, a silicon platform is one of the most attractive photonic integration platforms to implement compact, practical IMWP systems [51]. Nowadays, high performance active (modulators and detectors) and passive

(wavelength division multiplexers, demultiplexers, splitters, combiners, optical filters, and waveguides, etc.) photonic components are being fabricated and integrated together on SOI platforms with areas of thousands of square millimeters or less [40,41,48–51,61]. As an example, Zhang and Yao from the University of Ottawa have recently demonstrated a tunable bandpass MPF on a silicon chip consisting of a high-speed phase modulator, splitters, a thermally tunable high-Q micro-disk resonator, and a high-speed PD [61]. All the same, the remained barrier for the full integration of MWP systems on a single silicon chip is the realization of light sources on silicon platforms; this remains a fundamental practical challenge because silicon is an indirect energy bandgap and, therefore, poor light-emitting material [62,63]. As a result, no MWP platform has been reported to date which integrates all the required active (including sources and gain media) and passive photonic components in a single silicon chip. This issue was the main rationale for many researchers to migrate to III-V platforms which can offer the needed complete set of components on a single chip [21,45–47]. As an example, in 2016, Capmany et al. demonstrated an integrated MPF on an InP chip [46] involving a CW laser, an optical single-sideband (OSSB) modulator, a tunable optical filter, and a PD. The main associated problems of this implementation are the larger size, higher loss, and increased fabrication cost, as well as the difficulty in achieving seamless integration with electronics [59,61,64].

The richness of the silicon platform and its lowest production cost are driving forces for many researchers to strive for addressing the on-chip light source issue. Several groups of researchers around the world have deployed the so-called hybrid integration technique, i.e., the integration of III-V components on silicon platforms, to merge direct-bandgap materials with low-loss silicon active and passive photonic components [65–69]. Using this strategy, processed III-V lasers, gain chips, or even PDs can be optically connected readily to silicon photonic circuits, where the III-V device may be mounted either on top of the silicon substrate or next to it [69]. Recently, several research works have utilized “photonic” wire bonding techniques to enable highly flexible low-loss coupling of III-V devices to silicon photonic chips [69,70]. At the same time, in a parallel effort, many other research groups have been seeking novel approaches to overcome the inherent problem of silicon for the development of efficient light sources based on silicon [62,63,71,72]. Combining these results with the already available library of active and passive components in silicon technologies may establish the foundation toward the first all-on-silicon-chip high-performance IMWP functionalities, which will represent a revolution in IMWP.

So far, a handful of excellent reviews on the MWP and IMWP topics have been presented by Chen [73], Wang [74], and Lee [75], and the review articles by Gasulla [38], Yao [22], and Marpaung [3], to name a few. In particular, the comprehensive review article by Marpaung et al. in 2013 first covers the fundamentals of microwave photonics and then investigates the available platforms for IMWP. It then highlights the basic building blocks and reviews the advances on the IMWP until the publication date. More recent reviews on the IMWP subject focus on a limited range of applications [20,38,42,76–78].

In this article, we present a comprehensive review of the recent developments made since 2014 to date on the application of silicon photonic technology for MWP functions, i.e., the part of the IMWP literature that discusses silicon photonic devices for MWP applications. In particular, we focus on the design architectures for implementation of fundamental functionalities including modulation, AWG, filtering, true-time delay, phase shifting, beam steering, and frequency measurement, as illustrated in Figure 1. Much research during this period has been focused towards realizing IMWP functions at the system level using different techniques and improving figures of merit of MWP devices at the component level. We directly overview the results of the recent work on the topic and avoid the replication of the most basic material provided in previous reviews [3], e.g., fundamentals of MWP.

## 2. Signal Modulation and Manipulation

Over the past four years or so, the field of IMWP has experienced significant progress in three key functionalities for signal modulation, namely on-chip OSSB modulation, photonic assisted microwave

amplitude modulation, and photonic generation and modulation of ultra-wide-band (UWB) signals. We review recent important contributions in each of these fields in this section.

OSSB modulation is a scheme wherein one of the sidebands of an amplitude modulated signal is filtered out. OSSB modulation is a key operation in MWP systems such as radio-over-fiber transmission, photonic controlled phased array antennas, phase shifters, and optical vector network analyzers [13,32,79,80]. A novel OSSB modulation scheme based on a compact high-order integrated SOI coupled-resonator optical waveguides (CROW) filter was demonstrated in [81]. In particular, a sixth order CROW filter was designed with a ring radius of 4  $\mu\text{m}$  in a 220 nm SOI wafer. Inter ring coupling coefficients were optimized for a 70 GHz passband bandwidth with 20 dB sideband suppression. The RF responses of the resulting OSSB modulation generation after propagating across a dispersive medium was also calculated for a sixth order filter. RF power ripples did not exceed 2.5 dB for a 0 to 600 ps/nm dispersion range over a frequency span ranging from 40 MHz to 40 GHz. An SEM micrograph of the filter is shown in Figure 2a.

Figure 2b shows the measured amplitude and phase responses of the sixth order CROW filter. For comparison, theoretical responses are also shown. A tunable laser source was modulated via electro optic modulation to generate dual sidebands plus carrier. The fabricated filter then isolates one of the sidebands to generate an OSSB signal at the output. Finally, a PD was used to collect the OSSB signal. Figure 2c shows the spectrum of the output signal when modulated at 20 GHz.

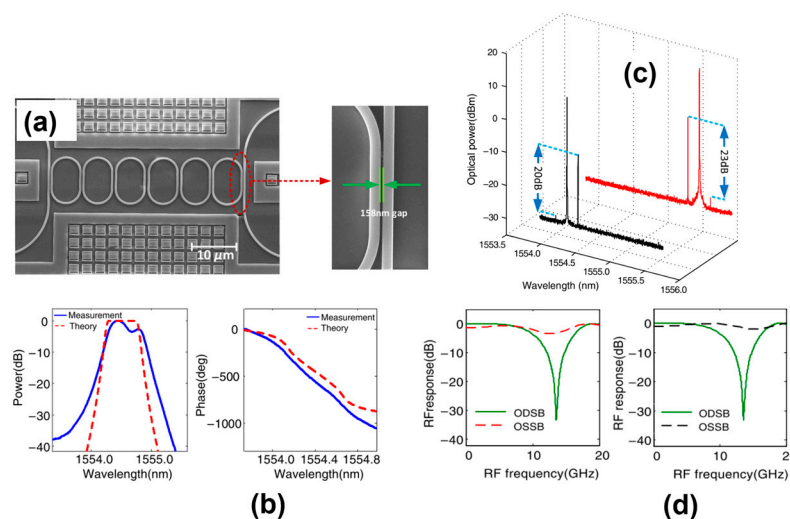


**Figure 2.** (a) Top-view scanning electron microscope image of the fabricated silicon-on-insulator microring coupled-resonator optical waveguides (CROW) filter reported in [81]. (b) Measured and theoretical ((amplitude (left) and phase (right)) response of sixth-order CROW filter. (c) Optical spectrum of the generated optical single-sideband (OSSB) signal with lower sideband suppression (black line) and upper sideband suppression (red line) when modulated at 20 GHz (after passing through the optical filter). (d) RF responses of the optical dual sideband (ODSB) and OSSB system with (left) upper sideband suppression (red dashed line) (right) lower sideband suppression (black dashed line). Courtesy of Xiaoke Yi [81].

Over 20dB sideband suppression was observed for both lower sideband and upper sidebands. OSSB is known to mitigate dispersion-induced power fading of the modulated signal, e.g., as the signal propagates through a dispersive optical fiber, as compared with the optical dual sideband (ODSB) modulation case. To compare the dispersion induced power fading with and without the filter, a linearly chirped fiber grating was used as a dispersive element. A significant dispersion-induced power fading of 33.2 dB was generated in an optical dual sideband (ODSB) system without the usage of an optical filter. On the contrary, the integration of the SOI filter allows the RF response to be nearly constant over a wide frequency range from 0 to 20 GHz, as seen in Figure 2d.

Photonic-assisted modulation and frequency multiplication of microwave signals have interesting applications in broad-band wireless access networks, software-defined radio, phased-array antenna, and radar systems etc. [82]. A simple and effective scheme to obtain frequency multiplied microwave signals and/or amplitude coded microwave signals based on a single integrated silicon Mach Zehnder modulator (MZM) was demonstrated in [83]. Specifically, a 50 Mb/s binary amplitude coded signal was generated in this experiment. Figure 3a illustrates the schematic of the proposed photonic assisted microwave signal modulation system using an integrated silicon MZM. Continuous-wave (CW) light from a tunable laser diode (TLD) was sent to the MZM. The microwave carrier signal and the binary coding signal  $s(t)$  were applied to the two RF ports of the MZM, respectively. The MZM was fabricated in a 220 nm SOI wafer, using 500 nm wide rib waveguides. Figure 3b shows the waveforms of the original 50-Mb/s baseband signal with a pattern of “110100101101001011”. The original 1-GHz microwave carrier is shown in Figure 3b. Figure 3c shows the modulated microwave (amplitude-shift keying (ASK)) signal.

In this work, the frequency of the generated microwave signals is limited by the operation bandwidth of the pin-type MZM used. To enable high frequency microwave signal multiplication and ASK signal generation, a high bandwidth, low half-wave voltage, and low loss MZM is needed; future improvement in integrated silicon photonic devices is needed to get efficient high frequency microwave signal modulation.

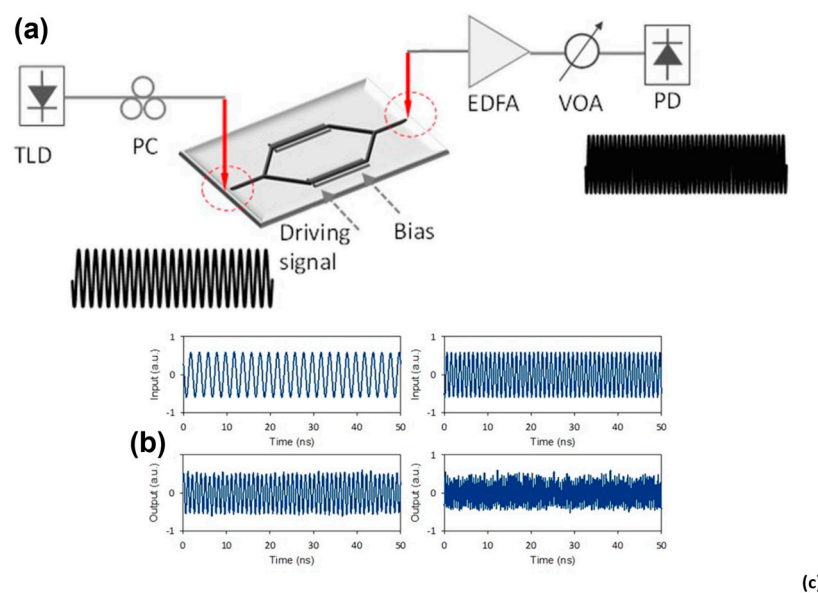


**Figure 3.** (a) Schematic illustration of the photonic assisted microwave frequency-modulation system using an integrated silicon Mach Zehnder modulator (MZM) reported in [83]; PC: polarization controller; EDFA: erbium-doped fiber amplifier; VOA: variable optical attenuator; TLD: tunable laser diode; PD: photodetector. (b,c) From top to bottom: waveforms of the original 50-Mb/s baseband signal, original 1-GHz microwave carrier signal, and the output microwave amplitude-shift keying (ASK) signal respectively. Courtesy of Jian Wang [83].

UWB technologies offers superior security and higher penetration ability in buildings, compared to short reach techniques like WiFi, Bluetooth etc. Although electrical generation of UWB signals in the 3.1 GHz to 10.6 GHz range can be achieved using electronics, the generation and processing of these signals in the optical domain is better suited for radio-over fiber (RoF) distribution networks [84]. An experimental demonstration of UWB monocycle pulse generation together with amplitude and bi-phase modulation based on a single microring modulator was demonstrated in [85]. The operation principle for simultaneous generation and modulation of UWB pulses is shown in Figure 4a,b. For pulse generation operation, the ring modulator converts the phase modulated light into its first order

derivative monocycle pulse; as shown in Figure 4a, when the laser wavelength is fixed, a monocycle pulse is generated through phase modulation to intensity modulation conversion. High speed amplitude modulation is achieved by carefully biasing the ring and applying an appropriate RF swing voltage. For bi-phase modulation, as shown in Figure 4b, a larger swing voltage is applied to shift the ring resonance, to fix the laser wavelength at the opposite slope of the resonance spectrum, hence the monocycle pulse will switch to the opposite polarity. The above scheme is based on reverse biasing a silicon microring pn junction modulator that exploits the free carrier plasma dispersion effect.

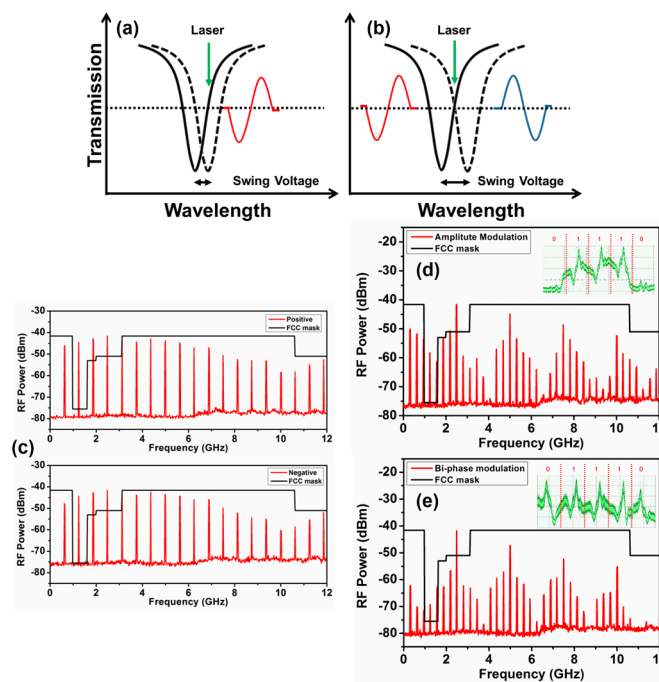


**Figure 4.** (a) Illustration of the principle for amplitude modulation of a monocycle pulse. (b) Principle for bi-phase modulation reported in [85]. (c) Electrical spectrum of the monocycle pulses with repetition rate of 625 MHz for both positive and negative polarity. (d) RF spectrum of the amplitude modulated monocycle pulses. Inset: waveform of the amplitude modulated pulses with a pattern of “01110” without zero padding. (e) RF spectrum of the bi-phase modulated monocycle pulses. Inset: waveform of the phase modulated pulses with a pattern of “01110” without zero padding. Courtesy of Hon Ki Tsang [85].

To generate UWB monocycle pulses from the ring modulator, the center of the ring resonance slope was biased at the laser output wavelength. Appropriately shaped monocycle pulses were observed in a sampling scope. The pulse waveform and the corresponding electrical spectrum are shown in Figure 4c. For both polarities, the central frequency was measured to be 4.68 GHz and the 10dB bandwidth was 6.88 GHz. By adjusting the bias and RF power, as discussed above, amplitude modulated UWB waveforms were generated, results shown in Figure 4d. A test bit pattern “01110” from a pattern generator was used without zero padding to investigate the modulation. Smooth transition from bit “0” to bit “1” could be clearly seen from the waveform and vice versa. The electrical spectrum of the amplitude modulated pulses is also shown in Figure 4d. The signal to noise ratio (SNR) for most of the frequency components was above 20 dB and the low frequency components also fit the FCC mask. Similarly, bi-phase modulated monocycle pulses were observed as shown in Figure 4e.

### 3. Phase Shifters

Broadband microwave phase shifters are one of the key components in microwave systems for applications ranging from phased array antennas, arrayed signal processors, microwave filters, and many more [4,35,86]. Compared to a purely electronic microwave phase shifter, an integrated

photonic phase shifter can operate at an ultra-compact form factor while offering higher bandwidth. Keeping with this trend, we investigate three implementations of an all optical microwave phase shifters on the silicon platform: a Bragg grating based approach offering dual capability of a phase shifter (PS) and a true time delay (TTD) unit [87], a scheme involving cascaded microring resonators that employs two photon induced thermal heating for phase tunability [34], and finally, a fully reconfigurable and fast PN junction-based PS [88].

An extremely compact ( $\approx 130 \mu\text{m}$  long) and simple device, integrated on a silicon platform, which can be reconfigured to operate both as a continuously TTD and as a PS over different GHz-level bandwidths was demonstrated in [87]. The device was based on a single uniform waveguide Bragg grating (WBG) with two phase-shift sections, operated in reflection. This architecture gives a sharp phase shift that can be exploited to generate either PS or TTD on the RF signal. The grating was designed in a 220 nm thick 500 nm wide silicon strip waveguide. The gratings were formed with 100 nm sidewall corrugations, with a grating period of 325 nm, as shown in Figure 5a.

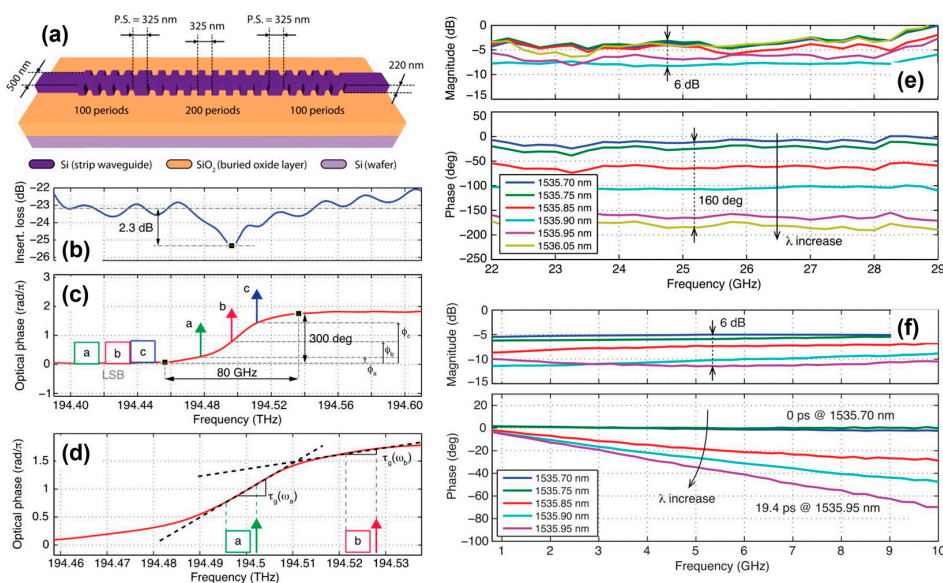


**Figure 5.** (a) Schematic of the dual-phase-shifted waveguide Bragg grating (DPS-WBG) reported in [87]. (b) DPS-WBG magnitude response, (c) Operation as phase shifter (PS), and (d) true time delay (TTD). (e) Complex (magnitude and phase) RF response for different phase shift values. (f) Complex (magnitude and phase) RF response for different true time delay values. Courtesy of Maurizio Burla [87].

The nearly flat response of the dual-phase-shifted waveguide Bragg grating (DPS-WBG) (ripple  $< 2.5 \text{ dB}$ ) over a band of more than 1.7 THz, with a shallow notch ( $\sim 2.3 \text{ dB}$ ) around the center of the reflection band, can be used to implement the desired RF photonics signal processing functions, see Figure 5b. The notch corresponds to a sharp transition in the phase response ( $\sim 300^\circ$  over 80 GHz). The DPS-WG response can directly implement an ultra-broadband PS. Considering an optical single-sideband with full carrier (OSSB + C) modulation scheme, by adjusting the optical carrier wavelength with respect to the resonance frequency of the DPS-WG, it is possible to provide the desired amount of phase shift  $\phi_c$  to the carrier only, while keeping the sideband phase unaffected, as shown in Figure 5b. The same device can be also employed as a microwave TTD with an instantaneous bandwidth of approximately 10 GHz. By simply varying the position of the carrier with respect to the resonance frequency, the phase transition around resonance of the DPS-WBG can be used to approximate a linear phase response with different slopes (Figure 5d), implementing a tunable TTD line. Figure 5e shows the experimentally obtained magnitude and phase response of the device for different carrier wavelengths, which shows the possibility to induce a continuously tunable and broadband RF phase shift of approximately  $160^\circ$ , over an instantaneous bandwidth between approximately 22 and 29 GHz. Figure 5f presents results corresponding to the TTD operation, showing continuous tunability

of the delay response in the range 0–19.4 ps, over an instantaneous microwave-signal bandwidth of approximately 1 to 10 GHz, as induced by simply tuning the optical carrier wavelength.

This scheme, although ultra-compact, suffers from low tuning range ( $160^\circ$ ) over a limited bandwidth (7 GHz) and high in-band power oscillations (6 dB). A full  $360^\circ$  phase shift is often required for implementing MPFs and in many other applications.

A full  $360^\circ$  optically tunable PS based on three cascaded passive microring resonators (MRRs) in SOI was experimentally demonstrated in [34]. The phase tuning is implemented based on the thermal nonlinear effect in the MRRs. By optically pumping the MRR at its resonance wavelength, two-photon absorption (TPA)-induced free carrier absorption (FCA) leads to an increase in temperature of the ring, at the local level, which changes its effective index due to the thermo-optic effect. Figure 6a shows the schematic of a microwave photonic phase shifter using a silicon-on-insulator microring resonator (SOI MRR). The OSSB modulated signal is sent to a MRR with the optical carrier located within the bandwidth of one of the MRR resonances to introduce a phase shift to the optical carrier. The phase shift is translated to the microwave signal at the output of the PD. It is easy to understand that compared to a single MRR, a cascade of 3 MRRs operating in an over coupling regime provides a full 360 phase shift near resonance. As mentioned above, The optical tunability of the phase shift  $\theta_0$  is achieved based on the thermal nonlinear effect where TPA-induced free carrier absorption (FCA) causes self-heating due to the strong thermo-optic coefficient of silicon. Three cascaded MRRs were fabricated on a 220 nm SOI platform. Each MRR had a radius of 20 microns, operating in the over-coupling regime. Figure 6b shows the measured phase response of the cascaded MRRs for different pump powers. The response without pumping is also shown. By increasing the pump power, the magnitude and phase responses are shifted to a longer wavelength. By placing the optical carrier (shown with black arrows in Figure 6b) of the OSSB signal in the bandwidth of the phase response, a phase shift will be introduced to the optical carrier as shown in Figure 6a. When the pump power is 27 dBm, the phase difference between optical carrier and sideband reaches its maximum value. This tunable phase shift can be used to obtain a phase shifted microwave signal when the OSSB-modulated signal is detected at the PD. Figure 6c shows the measured phase shift at different microwave frequencies. As can be seen, a full  $360^\circ$  phase shift with a bandwidth of 7 GHz from 16 to 23 GHz is achieved. As expected, the phase shift is independent of the microwave frequency.

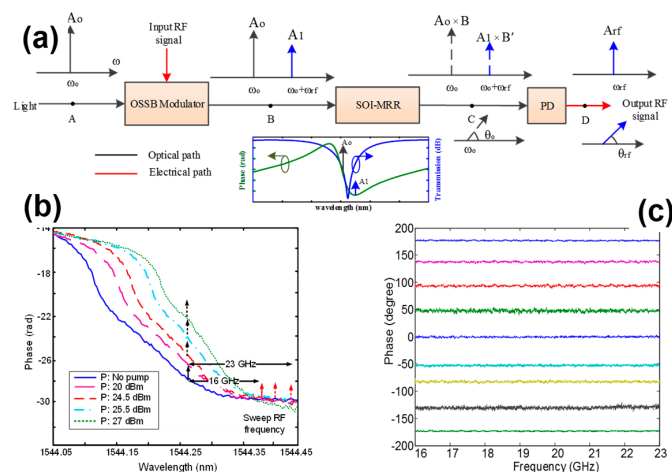


**Figure 6.** (a) Schematic of a microwave photonic phase shifter using an SOI MRR (silicon-on-insulator microring resonator) reported in [34]. OSSB: optical single-sideband, PD: photo-detector. Inset: the amplitude and phase responses of the SOI-MRR. (b) The phase response of the three cascaded microring resonators (MRRs) showing a net redshift of the phase response with the increase of the pumping power from 0 (no pump) to 27 dBm. (c) Measured phase shifts at different pumping power levels. Courtesy of Jianping Yao [34].

This scheme provides a full  $360^\circ$  phase shift using TPA induced self-heating. This process, although passive, does involve an additional high-power pump source—thus, effectively being “power-hungry” in its operation.

A SOI based photonic-integrated PS was reported in [88]. The PS simultaneously matches the demand for wide phase-shift range, broad bandwidth, low in-band power oscillations and fast reconfiguration speed. The schematic structure and the operation principle of the proposed MWP-PS are illustrated in Figure 7a. The core element of the architecture, highlighted in the dashed box of the figure, comprises an optical deinterleaver filter (ODF), an optical phase shifter (OPS), an optical coupler (OC), and a PD. OSSB signal is separated into carrier and the sideband by the ODF, a PN junction based PS provides the desired phase shift to the isolated carrier, which upon beating with the sideband at the on chip PD translates to generate a phase shifted microwave signal [23]. A PIC implementing the scheme within the dashed box of Figure 7a, was fabricated in SOI; a micrograph of the fabricated chip is shown in Figure 7b. The optical deinterleaver filter (ODF) was implemented using Microring loaded MZI. PN junction-based PS was used to achieve desired phase shift by applying proper reverse bias voltage. MMI based optical coupler was used to combine the phase shifted carrier and the modulated sideband. Two on-chip p-i-n Ge PDs were used to collect the MMI outputs. Figure 7c,d shows the measured magnitude and phase response over two different frequency bands namely 10 to 16 GHz range and 36 to 42 GHz range respectively. The curves illustrate flat phase shifts in the whole 6 GHz range spanning more than  $450^\circ$  for control signal range between 0 and  $-8$  V. A fast settling time below 1 ns was also reported for this phase shifter, thus allowing for fast reconfiguration speeds. Moreover, the periodic response of the MZI based ODF indicates that strong carrier-sideband isolation can be obtained around any RF carrier value that is an odd multiple of half the FSR. This property thus enables to suitably extend the described MWP-PS operation up to the mm-wave band, which is particularly appealing for several emerging applications, including high speed wireless communications in 5G systems.

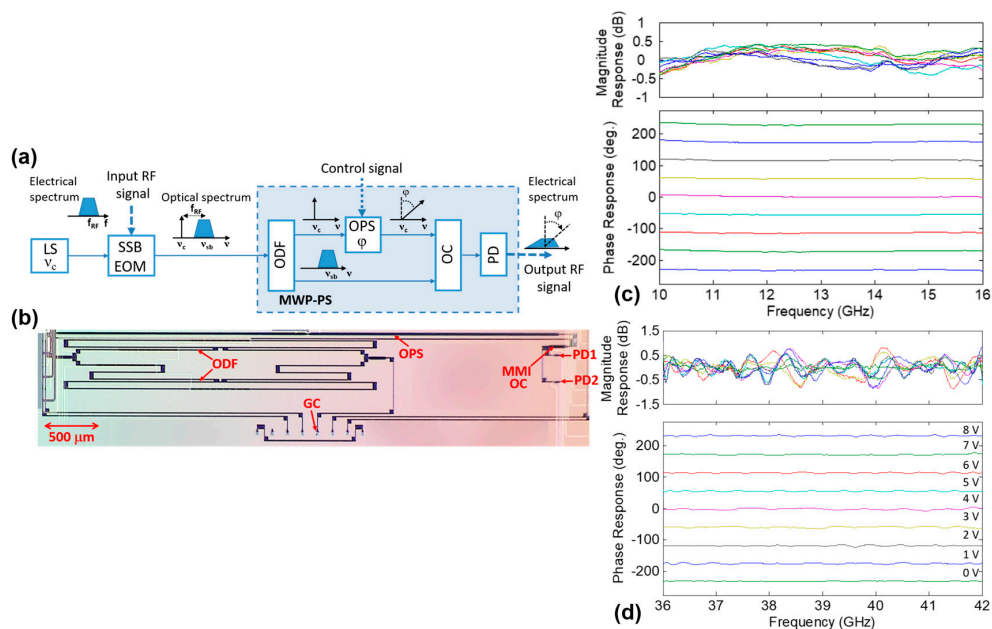


**Figure 7.** (a) Schematic and operation principle of the proposed photonic integrated phase shifter reported in [88]. LS: laser source; SSB EOM: single-sideband electro-optical modulator. In the scheme,  $f_{RF}$  represents the RF signal carrier frequency,  $\nu_c$  the optical carrier frequency,  $\nu_{sb}$  is the central optical frequency of the optical SSB modulated signal,  $\phi$  is the variable optical/RF phase shift. (b) Picture of the fabricated PIC; GC: grating coupler; MMI-OC: multi-mode interference optical coupler. Two PDs are connected to the two MMI outputs.

(c) Magnitude (top) and phase (bottom) response of the microwave photonics-phase shifter MWP-PS, as a function of the vector network analyzer (VNA) output RF frequency, over a 10-to-16 GHz frequency span. (d) Magnitude (top) and phase (bottom) response over a 36-to-42 GHz frequency span. Courtesy of Paolo Ghelfi [88].

#### 4. True Time Delay Line and Beam Steering

An important building block in a MWP system is an optical true time delay line (OTTDL). TTDLs provide a unique solution for broadband signal processing, such as tunable high-resolution microwave filters [89,90], beam forming in phased array antennas [91,92] etc. We review here three different implementations reported in the literature recently: a PN junction loaded microdisk cavity offering electrical tunability of group delay although suffering from lower bandwidth [93], an interesting demonstration involving subwavelength grating (SWG) waveguide which does not suffer from bandwidth limitations [94], and finally, a continuously tunable delay line using a cascade of switches and dual rings [95]. Moreover, we also review a  $1 \times 4$  beam steering system for phased array antennas (PAA) using 1-D grating waveguides based TTDLs [96].

A microdisk resonator (MDR) based electrically tunable delay line in SOI was demonstrated in [93], as depicted in Figure 8a. A MDR exhibits better performance in terms of footprint and light confinement factors compared to conventional micro ring resonators. However, conventional MDRs support multiple whispering gallery modes, which are not desirable for large finesse applications. Structure of conventional MDRs is not compatible with lateral PN junctions. Nevertheless, it is possible to incorporate lateral PN junction in a MDR cavity by surrounding the MDR with a slab waveguide as shown in Figure 8a. Introduction of a slab waveguide enables single mode operation as higher order modes leak out through the slab; secondly, the fundamental mode is further shifted away from the MDR sidewall, thus reducing the scattering induced losses. Moreover, a slab waveguide increases the overall area to implement the lateral PN junction. The proposed MDR was fabricated on a standard 220 nm SOI wafer using 248 nm DUV lithography and its optical performance is experimentally evaluated and is shown in Figure 8c. It is clear from the response that the MDR exhibits a single-mode operation with a free spectral range (FSR) of 28.85 nm. The electrical tunability was also demonstrated and an electro-optic frequency response with a 3-dB modulation bandwidth  $\sim 30.5$  GHz was measured. Thanks to the light-confinement capacity, an on-chip microcavity has a strong dispersion near the resonance and thus a large group delay. Figure 8e shows the measured group delay of the resonance WGM<sub>0,38</sub> in the fabricated MDR. As can be seen, the MDR presents a very large group delay of 68 ps. The ultra-compact footprint with a strong group delay fully demonstrates its potential in realizing an on-chip optical delay line. Figure 8f shows the electrical tunability of the group delay at three different wavelengths. As the reverse bias voltage is increased, the group delays at the three different wavelengths exhibit different variation. Such a change is obtained from the shift of the resonance at different bias voltages, which enables the electrical tunability of the achieved time delay.

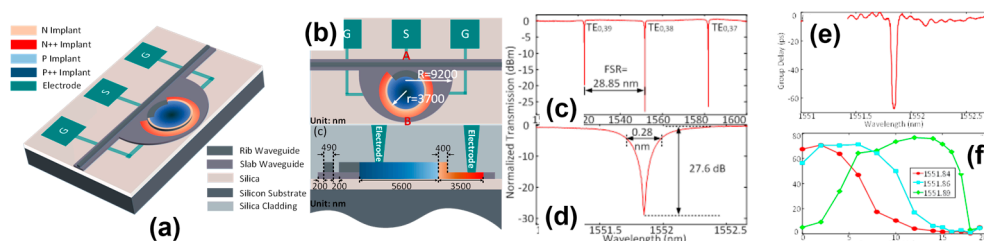


**Figure 8.** (a) Perspective view of an electrically tunable silicon-based on-chip microdisk resonator (MDR) reported in [93]. (b) Top view of the proposed MDR. (c) Measured transmission spectrum of the fabricated MDR, and (d) zoom-in view of the resonance of the fabricated MDR at the wavelength of 1551.84 nm. (e) Measured group delay of the resonance WGM<sub>0,38</sub> in the fabricated MDR and (f) electrical tunability of the group delay at three different wavelengths. Courtesy of Jianping Yao [93].

For an optical delay line, a wider operation bandwidth is highly desirable. By cascading several MDRs, a delay line with a wider bandwidth could be achieved.

The first proposal and experimental demonstration of an integrated SWG based index-variable OTTDL in SOI was reported in [94], see Figure 9. A SWG waveguide is a grating structure with a period that is smaller than the wavelength of light, which suppresses the diffraction effects, and behaves as a homogeneous medium with an equivalent refractive index [97]. By choosing the duty cycle ( $D$ ) of a SWG waveguide (refer to Figure 9a,b), group index can be effectively modified. Exploiting this unique property, a 4-tap straight SWG waveguide array configuration was used to induce time delay between two short pulses, as shown in Figure 9c. This index-variable OTTDL was designed to have  $\sim 10$  ps incremental time delay between the taps, achieved by varying the duty cycle of SWGs in each arm to be 60%, 50%, 40%, and 30%. By designing a different duty cycle value for each respective SWG waveguide branch, different optical paths among the waveguides, all having the same length ( $L$ ), can be engineered to control the temporal separation between the taps. Figure 9d shows the measured spectral response of the fabricated 4-tap OTTDL. The observed spectral periodicity features with  $\sim 0.9$  nm bandwidth correspond to an incremental time delay step of  $\sim 9$  ps between the taps. Figure 9e shows the generated time-domain output pulse sequence from a single input pulse measured using an oscilloscope. As shown in Figure 9c, the pulse propagating through the SWG waveguide with the lowest duty cycle (i.e.,  $D_4$ ) arrives faster compared to other pulses.

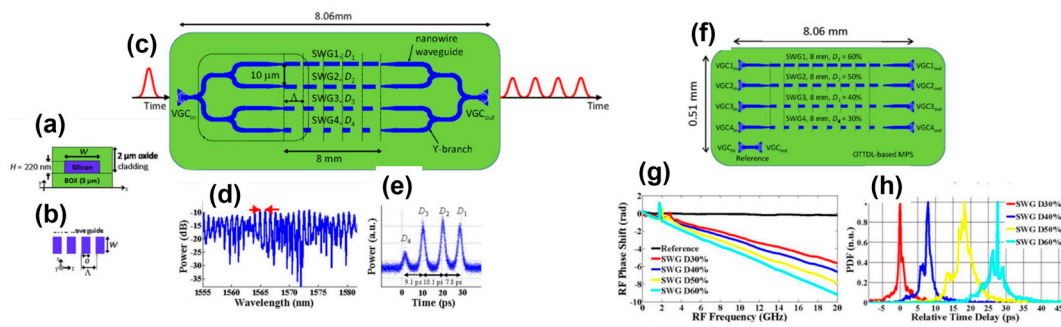


**Figure 9.** (a) The waveguide cross-section. (b) Parameters of the subwavelength grating (SWG) waveguide. (c) Schematic of the fabricated 4-tap optical true time delay line (OTTDL) structure based on SWG waveguides reported in [94]. (d) Measured power spectral response of the fabricated OTTDL. (e) Generated time-domain pulse train at the output of the fabricated OTTDL device in response to a single input optical pulse. (f) Array of 4 SWG waveguides with varying duty cycles from  $D_1 = 60\%$  to  $D_4 = 30\%$  in increments of 10%. (g) The measured RF phase shift when the modulated light is transmitted through different taps of the OTTDL. (h) The calculated probability distribution function (PDF) of the relative time delay given by the RF phase slope versus frequency shown in (g). The measured incremental time delay between the taps are 8.9 ps, 10.7 ps, and 7.9 ps, respectively.

Using SWG based OTTDL, a microwave phase shifter was also demonstrated. Figure 9f illustrates the schematic of an OTTDL based microwave phase shifter (MPS). It consists of an array of 4 SWG waveguides of the same length (8 mm), where the duty cycles of SWG waveguides in each arm were varied in 10% increments from  $D_1 = 60\%$  to  $D_4 = 30\%$ . A microwave signal modulated on an optical carrier will experience a different phase shift when propagating through different SWG waveguides. The measured RF phase shift as a function of frequency from 4 different SWG waveguides is shown in Figure 9g. The calculated probability distribution function (PDF) of the slope of the phase shift centered at different frequencies is shown in Figure 9h. Compared to other wavelength variable optical delay lines, this approach does not suffer from inherent RF bandwidth limitations as optical transmission window of SWG waveguides is constant over tens of THz.

Finally, experimental demonstration of a long-range continuously tunable optical delay line composed of a dual-ring slow light section followed by a switchable delay line section in an ultra-thin silicon platform was reported in [95]. Continuously tunable delay up to 1.28 ns was achieved thus

exhibiting a unique performance combination of tuning range, reconfigurability, resolution, and loss. Figure 10a shows the schematic of the entire delay line. The front dual-ring allows for the continuous fine-tuning of the delay using a differential resonance shift method. MZI based switchable delay line comprises of seven binary-delay stages, allowing for the discrete coarse-tuning of the delay. Figure 10b shows the cross section of the thermo-optic phase shifter used for fine tuning of delay in the rings. Figure 10c shows the simulated mode profile of an ultra-thin silicon waveguide (1  $\mu\text{m}$  wide X 60 nm thickness) for TE polarization. Such a thin waveguide is a good compromise in terms of loss, compactness, and detrimental nonlinear effect. A push-pull differential tuning method was used in the two-ring system to achieve fine tuning of delay from 0 to 23 ps with a bandwidth of 60 GHz. This was achieved by increasing the applied bias of one ring and reducing the bias on the other. In this way, the resonances shifted to opposite directions, with the original delay peak gradually divided into two, as seen in Figure 10e.

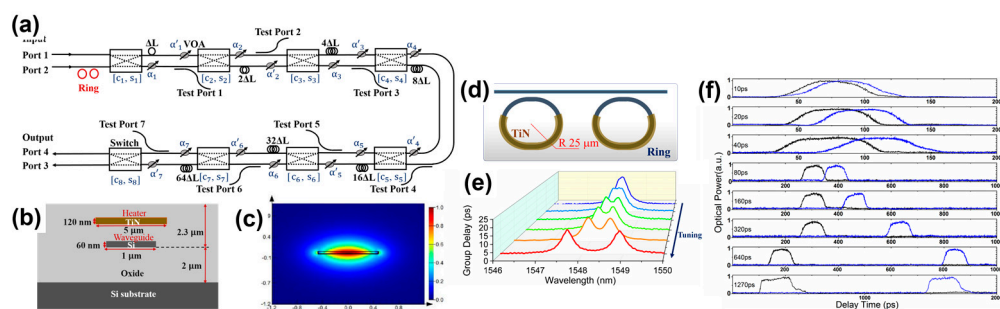


**Figure 10.** (a) Architecture of the continuously tunable optical delay line structure reported in [95]. (b) Cross-sectional structure of the ultra-thin waveguide with a titanium nitride (TiN) heater on top. (c) Simulated x-component of the electronic field distribution for the fundamental transverse electric (TE) mode. (d) Dual-ring slow-light delay line structure. (e) Evolution of the ring delay spectrum upon thermal tuning. (f) Optical pulse waveforms after passing through the switchable delay line. Black curves: reference pulses; blue curves: delayed pulses. (g) Optical pulse waveforms after passing through the longest optical path with delay fine tuning by the ring resonators. (h) Eye diagrams of a 30 Gb/s pseudo-random binary sequences (PRBS) signal after various delays; Gb/s: gigabits per second. Courtesy of Linjie Zhou [95].

The switchable delay line following the ring resonators is composed of seven delay stages, having incremental differential lengths of waveguides connected by pair of switches, the coarse delay tuning resolution  $\Delta t$  provided by this stage is 10 ps. Figure 10f shows the optical pulses after various digital delays. The operation wavelength was tuned to the off-resonance wavelength to eliminate the influence of the ring resonators. As seen, the relative delay increases exponentially from 10 to 1270 ps, depending on the length of the path selected by the switches. Delay fine tuning by the ring resonators when the switchable delay was fixed at maximum is also shown in Figure 10g. Eye diagram opening of a 30 Gb/s signal suggest that signal suffers little degradation due to increased insertion loss for a long delay.

True time delay lines play an essential role in PAA. The antenna consists of multiple elements, each with a phase shifter, which provides the desired interference condition so as to steer the beam in a particular direction. Compared to conventional electronic phase shifter based PAAs, photonics-based solutions employing TTDLs offer squint-free operation owing to large bandwidth and high speed.

A  $1 \times 4$  beam steering module based on an integrated 1-D grating waveguide was proposed in [96]. Compared to a 2D photonic crystal waveguide, the proposed 1D waveguide occupies 70% less space and thus allows for larger delays/unit length. Schematic of the proposed 1D grating waveguide in SOI is shown in Figure 11a. Figure 11b,c plot the typical electric field intensity distribution of the mode in the optimized 1D grating waveguide, which indicates that most energy is localized in the central waveguide. A 3D plane wave expansion method is used to calculate the band diagram. The idea is to obtain a relatively flat band with large slow-light bandwidth away from the band edge,

by tuning the values of width of the central waveguide ( $W_1$ ), the length ( $W_2$ ), the width ( $W_3$ ) of the teeth, and the period  $P$ . When the wavelength range is between 1540.20 nm and 1558.97 nm, 100 ps true time delay (TTD) can be readily obtained with less than 1 mm length of the 1D grating waveguide.

A  $1 \times 4$  beam steering system for PAA based on the proposed 1D grating waveguide was designed, as shown in Figure 11d. Modulated optical carrier was divided into 4 channels via MMI splitters and fed into four TTD lines of different lengths. Four phase shifts control the relative phase difference between the channels. Each channel has various lengths of the dispersive waveguide and normal strip waveguide. On-chip PDs were exploited to convert the optical signals back into electrical signals with delay information. The electrical signals were amplified and fed to PAAs. Based on relative time delay between adjacent channels, beam can be continuously steered as shown in Figure 11e. A tunable time delay between any adjacent TTD lines ranging from  $-38.62$  ps to  $38.62$  ps is achieved by tuning the wavelength from 1540.20 nm to 1558.97 nm. This continuously tunable TTDLs based on the 1D grating waveguide can provide a continuous beam steering angle from  $-67.84^\circ$  to  $67.84^\circ$  in the 8.0 GHz to 12.5 GHz range.

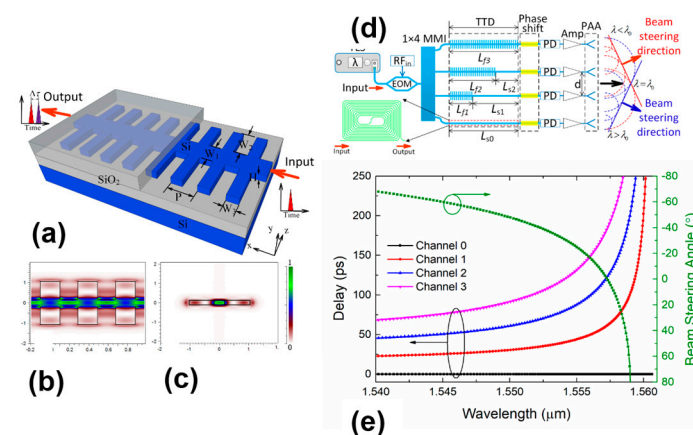


**Figure 11.** (a) Schematic configuration of the proposed 1D grating waveguide reported in [96]; (b) the electric field intensity distribution of the mode in the  $xz$  plane and (c) in the  $yz$  plane. (d) Wavelength continuously tunable beam steering system based on the 1D grating waveguide true time delay (TTD) lines. Amp: amplifier. Inset: schematic of the enlarged spiraled strip waveguide. (e) Delay time and beam steering angle versus wavelength for all four channels. The lengths of 1D grating waveguides are 0 mm, 1 mm, 2 mm, and 3 mm corresponding to channel 0, channel 1, channel 2, and channel 3. Courtesy of Jianyi Yang [96].

### 5. Instantaneous Frequency Measurement

Instantaneous frequency measurement (IFM) of unknown microwave and millimeter wave signals with low latency is a basic requirement in a wide range of applications, including modern biomedical instrumentation, electronic countermeasure (ECM), radar warning and electronic intelligence systems, development and testing of wireless systems [98–101]. A typical IFM system involves mapping the signal frequency to a more easily measurable quantity, such as power. Over the past couple of years, silicon based integrated photonic IFM systems have demonstrated great promise in terms of providing a low latency, high bandwidth, and low power alternative to existing state of the art electronic solutions. In the following section, we will review three different IFM systems. Out of the three, two systems rely on linear processing of signals using a disk resonator and a WBG respectively [102,103]. The third scheme relies on four wave mixing (FWM) and promises a record low measurement error [104].

A flexible and simple photonic approach to microwave frequency measurement with adjustable measurement range and resolution was proposed and experimentally demonstrated based on a low-loss silicon MDR in [102]. The schematic diagram of the MDR-based photonic microwave frequency measurement system is shown in Figure 12a. The OSSB signal, with microwave frequency  $\omega_{RF}$ , was fed to the MDR, which acts as a tunable notch filter. The optical spectrum of the MDR

was mapped to the RF spectrum by a PD. By shifting the optical carrier, different MPF responses can be obtained to calculate the corresponding amplitude comparison function (ACF), as shown in Figure 12b,c. An ACF represents a unique relationship between detected power of the RF signal and its frequency, so it forms the cornerstone of all photonic based IFM systems. The relationship between the power ratio and microwave frequency is unique in the monotonic increasing region ( $\omega_{RF1}/2\pi - \omega_{RF2}/2\pi$ ) of the ACF, as shown in Figure 12c. High Q MDR is essential to ensure different microwave power penalties for two closely space laser wavelengths. A 10  $\mu\text{m}$  bend radius MDR was fabricated using 500 nm wide rib waveguide on a 340 nm thick SOI wafer. By tuning the central wavelength of the tunable laser source to  $\lambda_1$ (1554.098 nm),  $\lambda_2$  (1554.066 nm), and  $\lambda_3$  (1554.018 nm) respectively, three MPF responses whose notch frequencies were 9, 12, and 19 GHz, respectively were obtained and is shown in Figure 12d. Figure 12e,f shows the measured and theoretical ACF between  $\lambda_1, \lambda_2$ , and  $\lambda_2, \lambda_3$  respectively. As observed from the plots, there is an inherent trade off between resolution and range of frequency measurement. However, having three MPFs allows for control over both resolution and range of frequency measurement, as seen in Figure 12g: for a wide frequency range of 9–19 GHz, RF frequency could be measured with an error of  $\pm 0.1$  GHz.

MDR based method of frequency measurement reduces system complexity by only employing a single laser source, modulator and a PD, but it does have some limitations. Frequency measurement of RF signal with low frequency is limited by the Q factor of the MDR; very high Q factor ( $>1 \times 10^5$ ) MDRs are required for low frequency detection using this technique. Secondly, to have better resolution (low error) a-priori knowledge of incoming microwave signal is needed to accordingly select the two laser wavelengths, to calculate the corresponding ACF.

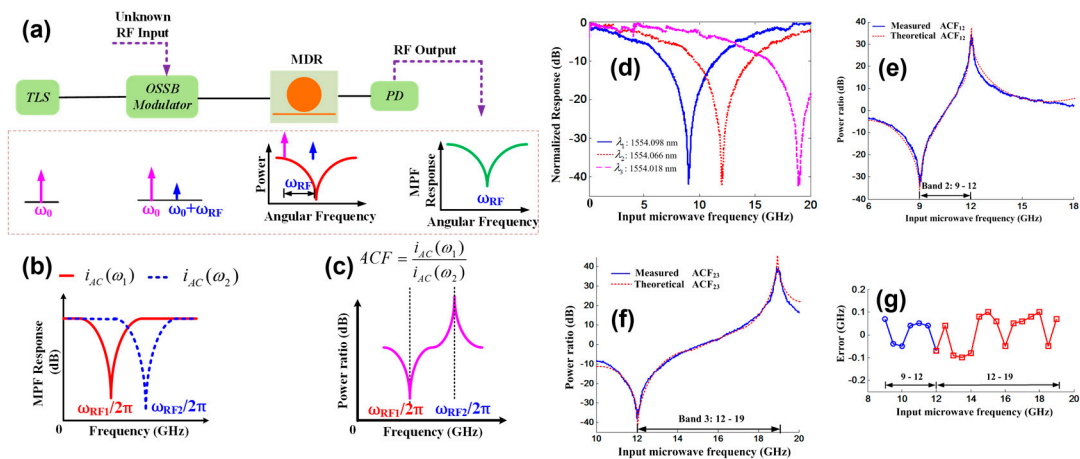


**Figure 12.** (a) Schematic diagram for microwave frequency measurement reported in [102]. (b) and (c) Calculated microwave photonic filter (MPF) responses and amplitude comparison function (ACF), respectively. (d) Measured MPF responses for three different wavelengths of  $\lambda_1, \lambda_2, \lambda_3$  (e) Theoretical and measured  $ACF_{12}$  when the system is operating at  $\lambda_1$  and  $\lambda_2$ , respectively. (f) Theoretical and measured  $ACF_{12}$  when the system is operating at  $\lambda_2$  and  $\lambda_3$ , respectively. (g) Measurement range and error for the three wavelengths of  $\lambda_1, \lambda_2, \lambda_3$ . Courtesy of Jianji Dong [102].

Next, a single, very simple and compact optical WBG filter on-chip was employed to perform frequency measurement in [103]. The filter was realized using a phase shifted WBG (PS-WBG) in a complementary metal-oxide-semiconductor (CMOS)-compatible silicon on insulator platform. Figure 13a shows the schematic of the 65  $\mu\text{m}$  long PS-WBG filter, where the input and output of the filter were accessed using grating assisted couplers. A Y-branch was used to access both the transmission and the reflection responses of the filter. The grating was simultaneously operated in transmission and reflection to provide two separate frequency responses. The simulated and measured responses for

both transmission and reflection ports are shown in Figure 13b,c. Based on these responses, an ACF is defined as detailed in Equation (1):

$$ACF(\omega) = \frac{P_{TX}(\omega)}{P_{RX}(\omega)} \quad (1)$$

The microwave frequency to be determined is mapped to the corresponding microwave power by this ACF. The scatter plot in Figure 13f shows the microwave frequency estimated using the IFM system versus the actual input frequency for each of the test tones, as well as the residual measurement error. The figure shows that the system can measure tones up to 32 GHz with a mean square error of 773 MHz. The degradation of noise figure of the photonic link leads to such uncertainty. In this work, dynamic frequency identification of a frequency hopping signal was also carried out using the same PS-WBG based filter. Readers are directed to [15] for detailed results.

Last, a low-latency instantaneous frequency measurement system using on-chip four wave mixing (FWM) in silicon was experimentally demonstrated in [104].

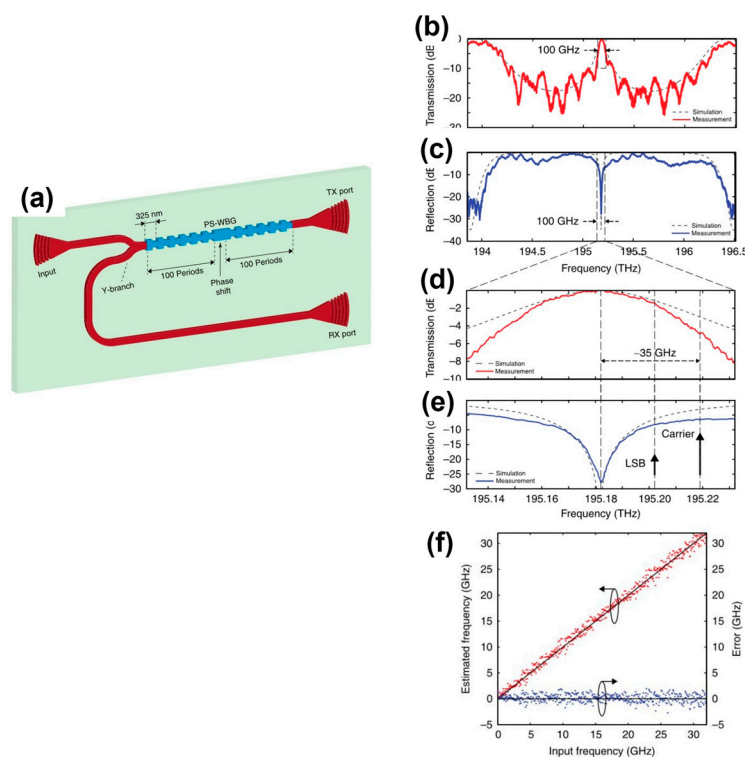


**Figure 13.** (a) Schematic of the silicon phase shifted WBG (PS-WBG) employed as a linear-optics frequency discriminator reported in [103]. TX port, transmission port; RX port, reflection port. Simulated (dashed line) and measured (solid line); (b) linear optical transmission and (c) reflection spectral responses of the PS-WBG; (d,e) zoom with overlapped OSSB+C spectrum. (f) Estimated frequency (red dots) and corresponding error (blue dots).

A record low 0.8% error over a 40 GHz measurement bandwidth was reported, using an ultra-low loss 35 cm long, thick silicon waveguide. Schematic of the FWM based IFM system is shown in Figure 14a,b. An unknown RF frequency modulates two CW carriers at different frequencies  $\omega_1, \omega_2$ . Signals are demultiplexed using a coarse wavelength-division multiplexer (CWDM). One signal is delayed by  $\Delta t$  relative to the other. Signals are recombined once again and are sent through a long ultra-low loss silicon waveguide wherein they interact through FWM. There are two FWM processes that occur simultaneously inside the waveguide, as shown in Figure 14b, giving rise to two separate pairs of idler sidebands. The first is a degenerate FWM (DFWM) process, which gives rise to a delayed pair of idler sidebands. The second process is a nondegenerate FWM (NDFWM) process where the generated idler pair is a copy of the non-delayed optical signal. The total sideband idler

field is a coherent sum of two separate idler fields with a differential delay of  $\Delta t$ , resulting in an interference effect.

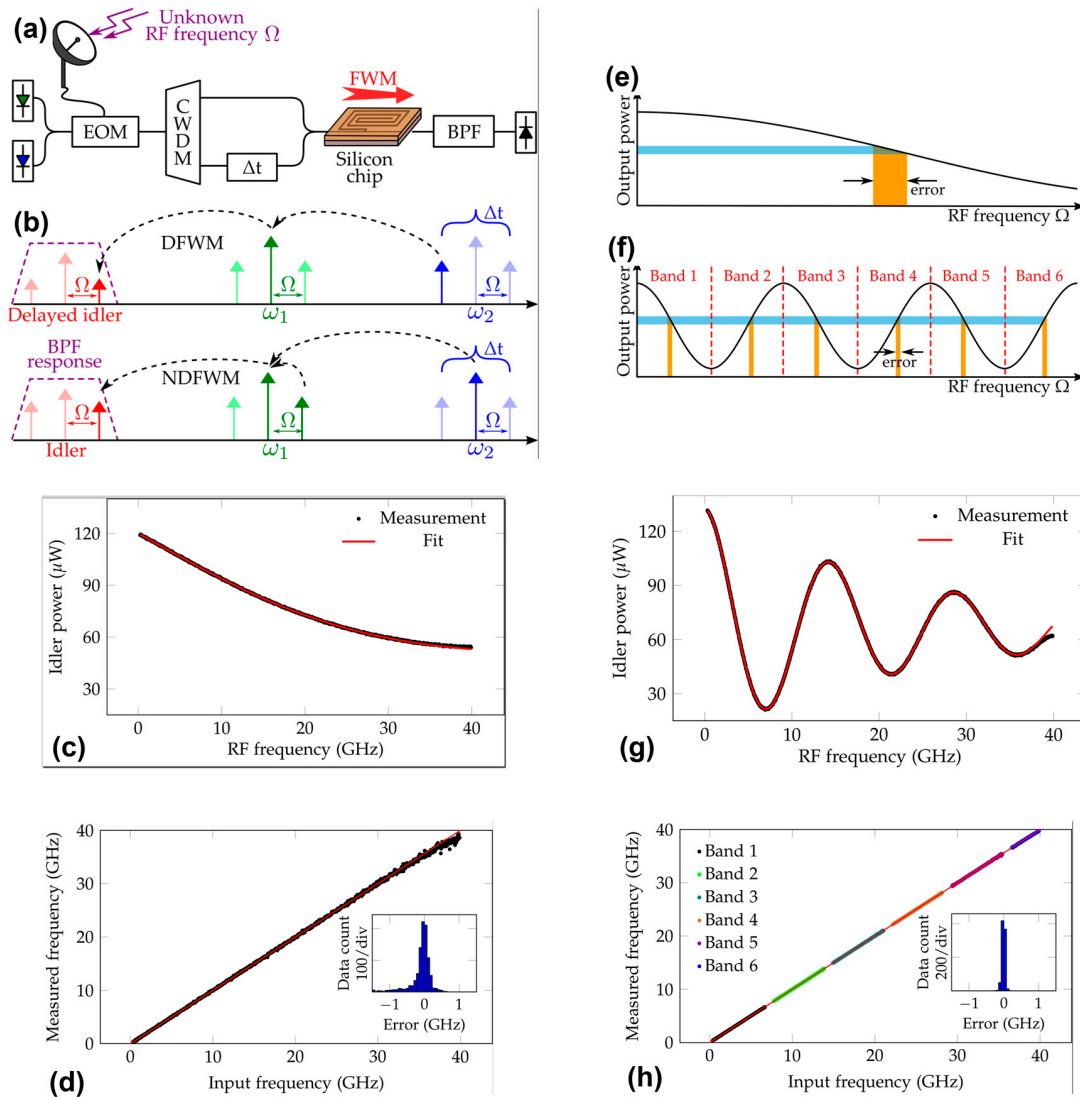


**Figure 14.** (a) Schematic of the on-chip four wave mixing (FWM)-based instantaneous frequency measurement (IFM) system reported in [104].  $\Delta t$ : tunable delay element; BPF: optical bandpass filter. (b) DFWM and NDFWM mixing processes between the two channels. (c) IFM RF system response with  $\Delta t = 8.3$  ps. (d) Frequency estimation measurement over a single 40 GHz frequency band (inset, histogram of the frequency measurement error; rms value = 318.9 MHz). Reconfiguration of the IFM system response between (e) a high-bandwidth/error state (low  $\Delta t$ ) and (f) a low-bandwidth/error state (high  $\Delta t$ ). (g) IFM system response with  $\Delta t = 69.4$  ps. (h) Frequency estimation measurement for six separate 7.2 GHz frequency bands (inset, histogram of the frequency measurement error; rms value = 40.2 MHz). Courtesy of David Marpaung [104].

Using a bandpass filter, the total idler field can be extracted, and its power can be measured with a PD. This result allows for a one-to-one mapping between the idler power ( $P_{idler}$ ) and the unknown RF frequency ( $\Omega$ ) as shown in Equation (2), for some constants A and B with  $A > B$ .

$$P_{idler} = A + B\cos(\Omega\Delta t) \tag{2}$$

The measurement along with the theoretical fit using Equation (2) is shown in Figure 14c,d. Increasing  $\Delta t$  delay can improve the measurement resolution at the cost of reduced bandwidth as

shown in Figure 14e,f. Using a  $\Delta t$  of 69.4 ps, the system response and the theoretical fit are shown in Figure 14g. Each linear region of the system response corresponds to a 7.2 GHz wide band, see Figure 14h, thus exhibiting low estimation error.

In this work, a fully integrated FWHM platform in SOI was also presented as an outlook. The proposed platform would house a tunable time delay unit, phase modulator, intensity modulator and an arrayed waveguide grating in the thin part of the chip whereas thick silicon part of the chip would be used to fabricate the low loss FWM waveguide, PD and a bandpass filter. Readers are directed to [104] for more details. This novel approach has certainly opened the door for a fully reconfigurable, monolithic IFM receiver.

## 6. Microwave Photonic Filters

MPFs are of great importance to process random and unpredictable microwave signals in numerous microwave settings, e.g., radars, satellites, and wireless communication systems, bringing supplementary advantages inherent to photonics, particularly extremely wide tunability, which transcends the abilities of electronic RF filters. A significant amount of efforts has been devoted for developing high performance MPFs in the past. The evolution of integrated microwave photonic filters (IMPFs) has been specifically helped by the remarkable linear and nonlinear filtering properties of integrated photonic devices, such as nanowires, waveguide Bragg gratings, interferometers, and micro-resonators. In this context, much work has been undertaken based on the optical-to-RF mapping concept in which the spectral response of an optical filter is linearly mapped to the RF field. Alternatively, a handful of research works have exploited the nonlinear effects in nanowires, such as stimulated Brillouin scattering (SBS), to implement a microwave filter response. To tune the central frequency of the implemented linear and nonlinear-based MPFs, two mechanisms are typically used: 1- tuning the optical carrier wavelength and 2- tuning the transmission spectrum of the optical filter using nonlinear effects, such as thermo-optic effects, the opto-mechanical effects, Kerr effects, and TPA.

A summary of silicon-based IMPF demonstrations since 2014 until mid-2018 is shown in Table 1, targeting to meet key performance metrics, such as high rejection ratio, high selectivity, wide frequency tunability, low power consumption, and low footprint. Many of these approaches have been mainly based on single micro-resonators [49,61,105–113], in either of ring, disk or ultra-compact photonic crystal nanocavity shapes. A few, however, have focused on more elaborated designs involving more than one micro resonator or incorporating Mach-Zehnder interferometers (MZIs) [114–117]. A few works also have investigated the use of other photonic devices such as nanowires, photonic crystal MZIs, optomechanical cavity-waveguides, and WBGs [50,118–123].

**Table 1.** Selected reported results for silicon-based integrated microwave photonic filter (MPF).

Year	Filter Type	Key Component(s)	Tuning Mechanism	Merits	1 <sup>st</sup> Author [Ref]
2018	Bandpass	MDR	Thermo-optic effect (TOE)	All-on-chip MPF, full width at half maximum (FWHM) = 1.93 GHz, tuning range (TR) = 3–10 GHz	Zhang [61]
2017	Bandpass	PhC microcavity	Tunable laser (TL), combined optical nonlinear effects (CONLE)	Ultracompact, all-optical tuning, TR = 13.9–24.0 GHz	Long [105]
2018	Bandpass	Ultra-high-Q micro-ring resonator (MRR)	TOE	FWHM = 170 MHz, RR = 25 dB, TR = 2–18.4 GHz	Qiu [106]
2014	Notch	MDR	TL	Rejection ratio (RR) = 40 dB, TR = 6–18 GHz	Li [107]
2015	Notch	MRR	CONLE	All-optical tuning, TR = 8.79–15.64 GHz	Long [108]
2017	Notch	Opto-mechanical	Opto-mechanical effect and optically induced TEO	All-optical tuning, TR = 6–19 GHz	Li [109]

Table 1. Cont.

Year	Filter Type	Key Component(s)	Tuning Mechanism	Merits	1 <sup>st</sup> Author [Ref]
2018	Bandpass	Double MMRs	TOE in both rings	Shape-invariant tuning, RR = 22 dB, TR = 6–17 GHz	Song [114]
2018	Notch	MRR assisted by two Mach-Zehnder interferometers (MZIs)	TOE	RR = 63.2 dB FWHM = 780 MHz TR = 0–40 GHz	Liu [115]
2016	Bandpass	Cascaded MRRs	TL+TOE	TR = 19–40 GHz Tunable FWHM = 5.5–17.5 GHz	Liu [116]
2015	Notch	MRR	TL	Tunable RR = 14.5–61.5 dB, TR = 12.4–30.6 GHz	Long [49]
2017	Notch	PhC microcavity	TL	Tunable RR = 11.8–62.1 dB, TR = 12.4–30.6 GHz	Long [110]
2015	Notch	Nanowire	TL	FWHM = 98 MHz, RR = 42 dB, TR = 14.7–19.8 GHz	Casas-Bedoya [118]
2016	Channel equalizer	Two-tap MZI with PhC coupler	TOE	RR = 18 dB, sign change of the weighting coefficients	Gay [119]

Representative results from one micro-resonator can be found in [61,105–110]. These MPF proposals share the same operation concept, shown in Figure 12. Figure 12a shows the schematic diagram of a typical single all-pass micro-resonator and its power transmission spectrum. The transmission spectrum of a single cavity resonator can be expressed as [124]

$$T_s = \frac{I_{out}}{I_{in}} = \frac{a^2 - 2ar\cos\varphi + r^2}{1 - 2ar\cos\varphi + (ar)^2} \quad (3)$$

where  $\varphi = \beta L = (2\pi n_{eff}/\lambda)L$  is the single-pass phase shift, with  $L$  being the round-trip length,  $\beta$  the propagation constant of the circulating mode,  $n_{eff}$  the waveguide effective index and  $\lambda$  the wavelength.  $a$  is the single-pass amplitude transmission, including both propagation loss in the ring and loss in the couplers. It relates to the power attenuation coefficient  $\alpha$  [1/cm] as  $a = \exp(-\alpha L)$ .  $r$  is the self-coupling coefficient. We can similarly define  $\kappa$  as the cross-coupling coefficient, and therefore,  $r^2$  and  $\kappa^2$  are the power splitting ratios of the coupler. For ideal cavities with zero attenuation,  $a \approx 1$ , the transmission is unity for all values of detuning  $\varphi$ , i.e., for all values of wavelength in a given device. Under critical coupling, i.e., when the coupled power is equal to the power loss in the ring  $r = a$ , the transmission at resonance falls down to zero, as shown in Figure 12a.

For MPF applications, one of the important design parameters of resonators is the Q-factor (or quality-factor). Q-factor of a resonator is a measure of the resonator capacity to store light, and is defined as the ratio of the energy stored to the energy dissipated in the resonator. In practical applications, the Q-factor of the microresonator translates into the narrowness of the resonance linewidth, and depth of the optical intensity resonance. This important design parameter of micro-resonators, therefore, directly determines the selectivity and extension ratio of the implemented MPF. Q-factor of a micro-resonator can be calculated as [124]

$$Q = \frac{\lambda_{res}}{FWHM} = \frac{\pi n_g L \sqrt{ra}}{\lambda_{res} - (1 - ra)} \quad (4)$$

where  $n_g$  is the group index,  $\lambda_{res}$  is resonance wavelength of cavity and  $FWHM$  is the full width at half maximum of the resonance spectrum. For MPF implementations, it is typically desired to realize a micro-resonator with a high Q-factor. Also, when nonlinear effects are involved in the resonators, a higher Q/V ratio (V being the modal volume of the resonator) is essential as it determines the strength of various light-matter interactions in the micro-resonator.

MPF approaches based on a single micro-resonator (ring, disk or ultra-compact photonic crystal nanocavity shapes) utilize the optical-to-RF mapping concept where the optical micro-resonator spectrum is linearly mapped to the microwave domain. The usual implementation of this concept can follow two schemes as shown in Figure 12a,b. In both schemes, a microwave signal is first modulated on a signal optical carrier, and then processed by a resonator and detected by a PD. However, the modulation format determines the bandpass or bandstop (notch) nature of the MPF [61,105–110]. To be specific, in Figure 12b, we first assume that an RF signal is modulated onto an optical carrier (CW light) of frequency  $f_s$  by the phase modulation technique. Assuming a small-signal sinusoidal drive signal of frequency  $f_{RF}$ , the optical field at the output of a phase modulator (PM), using the Jacobi–Anger expansions, can be written as [107]

$$A(t) = J_0(\beta)\exp(j\omega_s t) + J_1(\beta)\exp(j(\omega_s + \omega_{RF})t) + J_{-1}(\beta)\exp(j(\omega_s - \omega_{RF})t) \quad (5)$$

where  $\omega_s = 2\pi f_s$  and  $\omega_{RF} = 2\pi f_{RF}$  are the angular frequencies of the input optical carrier and applied drive signal, respectively.  $\beta = \pi V_{RF}/V_\pi$  is the modulation index, and  $V_\pi$  and  $V_{RF}$  are the half-wave voltage of the PM and the amplitude of the driving signal, respectively.  $J_n$  is the  $n$ th order Bessel function of the first kind in which  $J_1 = -J_{-1}$ , indicating that the two generated lower and upper sidebands are 180° out of phase, i.e., there is an anti-phase symmetry. The phase modulated signal (optical double sideband (ODSB) signal) is then launched into a micro-resonator. Note that the optical carrier is adjusted to locate around the left or right edge of the notch resonance frequency; in Figure 12 we assume it is located on the left edge.

The output signal of the resonator is the directed into a PD. The two sidebands beat with the optical carrier separately and generate an RF signal. The electrical current after PD could be expressed as:

$$i_{ac}(t) \propto \{J_0(\beta)J_1(\beta)\cos(\omega_{RF}t) - J_0(\beta)J_1(\beta)\cos(\omega_{RF}t)\}. \quad (6)$$

When the upper sideband of the signal is filtered by the resonator (by falls in the notch resonance), the anti-phase symmetry will break and the optical carrier and the lower sideband beat each other and generate a microwave signal after photo-detection. Otherwise, if the upper sideband is not filtered by the resonator, both sidebands would beat with the optical carrier separately, and generate two microwaves with a phase difference of  $\pi$  (see Equation (6)) and fully cancel each other; thus, no microwave signal will be generated at the output of the PD. Hence, with the optical-to-RF mapping, a bandpass MPF with a central frequency of  $\omega_{RF}$  would be achieved, as shown in Figure 15b. Note that, however, in practice micro-resonators introduce a non-ideal, non-zero phase outside its notch bandwidth which prevents full cancellation of the anti-phase modulation sidebands, and consequently degrades slightly the rejection ratio and shape factor of the MPF.

In the second filtering scenario, if we employ the OSSB modulation instead to modulate the RF signal onto an optical carrier (CW light), the outcome filter would be a notch filter, as depicted in Figure 15c. OSSB is typically carried out by using a rectangular bandpass filter after a phase modulator to remove the lower or upper sideband of an ODSB signal in Equation (5). An OSSB signal, assuming lower sideband removal, can then be expressed as:

$$A(t) = J_0(\beta)\exp(j\omega_s t) + J_1(\beta)\exp(j(\omega_s + \omega_{RF})t). \quad (7)$$

The OSSB signal after being processed by a micro-resonator is photo-detected and the electrical current after the PD could be then expressed as:

$$i_{ac}(t) \propto \{J_0(\beta)J_1(\beta)\cos(\omega_{RF}t)\}. \quad (8)$$

As can be inferred from Equation (8), when the sideband component  $\omega_s + \omega_{RF}$  is aligned at the notch resonant of the resonator, the MPF response reaches a minimum, otherwise it is a constant. Thus, a notch MPF with central frequency of  $\omega_{RF}$  could be realized.

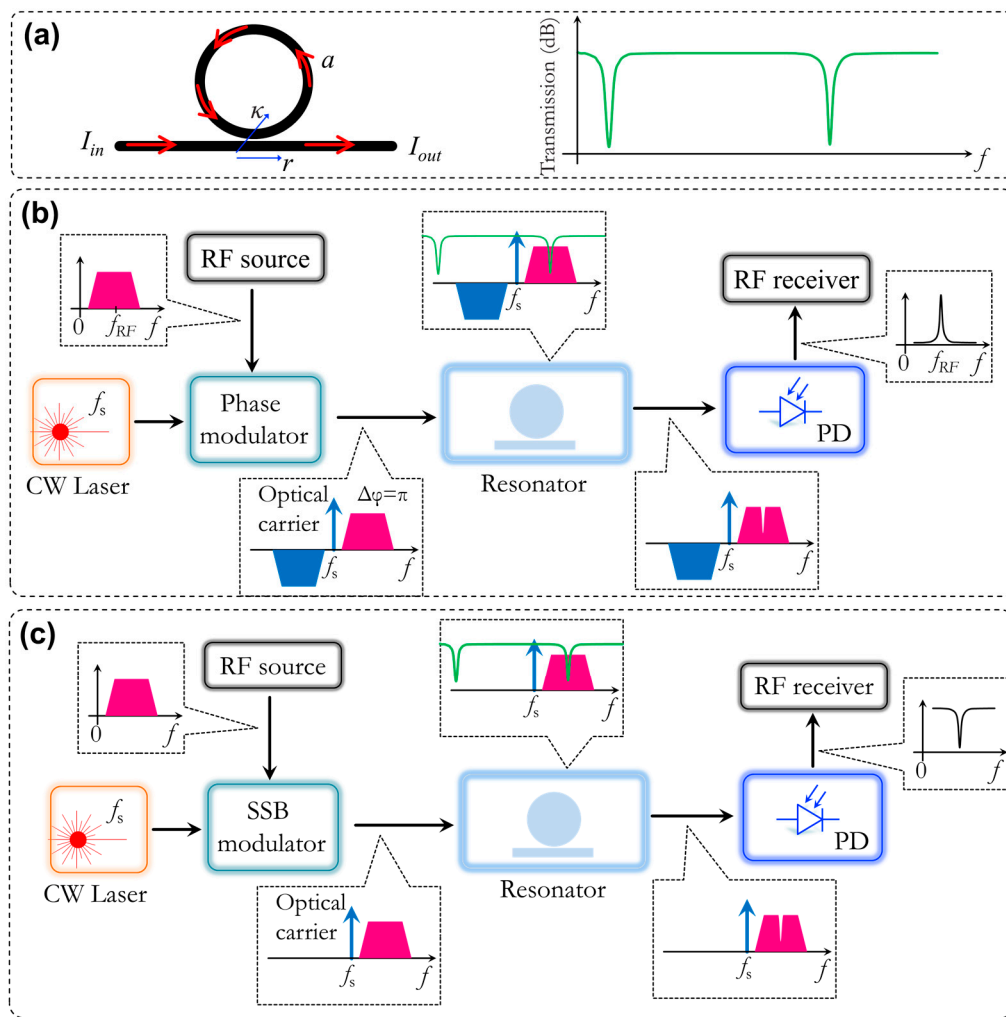


**Figure 15.** Operation concept of MPFs based on a single micro-resonator (a) All-pass micro-resonator and its power transmission spectrum. Schematic illustration of the schemes for (b) bandpass and (c) notch MPF implementations based on optical-to-RF mapping concept.

As mentioned above, two general mechanisms have been employed in the reported IMPFs to tune the frequency of the MPFs [61,105–110]. The primary mechanism is to tune the optical carrier wavelength (changing the source wavelength) with respect to the resonance wavelength of the micro-resonator (see Figure 16a). This tuning technique requires a wavelength tunable CW laser with a sub-gigahertz resolution. Alternatively, a frequency-tunable MPF can also be achieved by tuning the resonance wavelength of a micro-resonator using nonlinear effects, such as thermo-optic effects, TPA, Kerr effects, and opto-mechanical effects. The nonlinear effects will alter the effective optical path (through refractive index change) of the micro-resonators and subsequently cause the resonant-frequency shift in them, leading to the change of frequency difference between the optical carrier and resonant frequencies. To use thermo-optic effects alone, micro-resonators are equipped by metallic micro-heaters located on the top of them. By adjusting the electrical voltage applied to the metallic micro-heater, the resonance frequency of micro-resonators and consequently MPF are tuned (see Figure 16a). There have been also a few works that report the realization of an all-optical tuning mechanism based on some combined optical nonlinear effects. As such, the central frequency of a MPF can be flexibly tuned by changing the power of either the carrier light (Figure 16c) or an assistant pump light (Figure 16c). Indeed, when a strong light is propagated into a silicon waveguide, it is partially absorbed through the TPA process, which will introduce refractive index change proportional to the light intensity (Kerr effect). Through the TPA process, free carriers can be excited which leads to extra

absorption and an associated refractive index change (free carrier dispersion, FCD). By the energy conservation law, the optical energy absorbed in TPA and FCA processes is eventually converted into thermal energy, resulting in heating of the structure and inducing a thermal refractive index change.

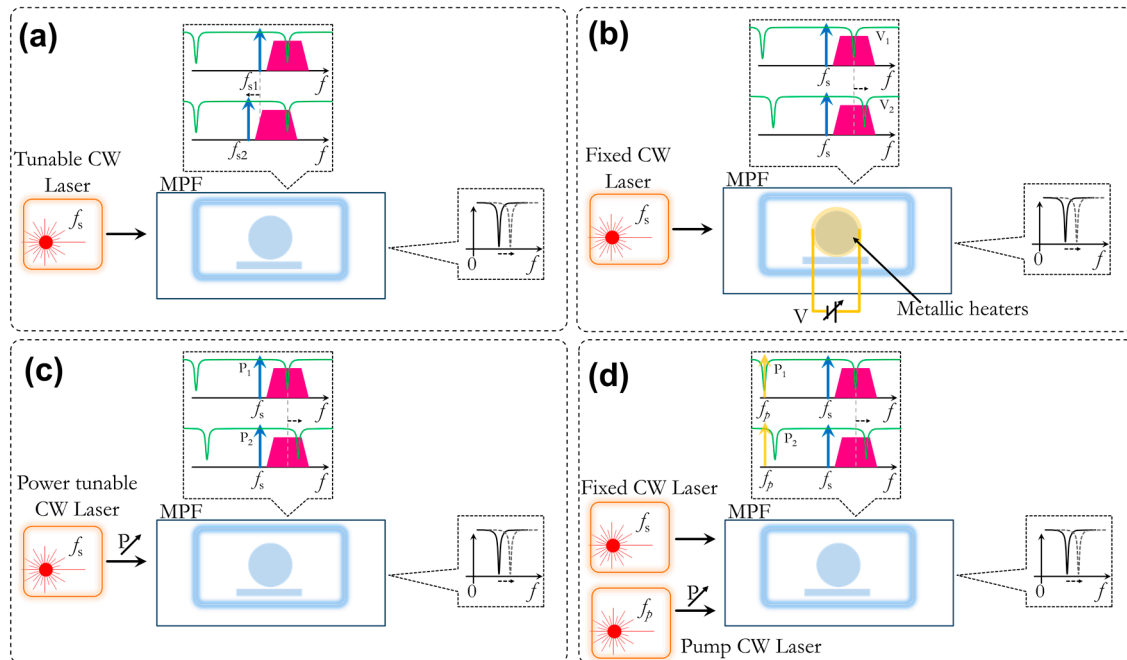


**Figure 16.** General frequency-tuning mechanisms for MPFs. (a) Tuning the optical carrier wavelength using a wavelength-tunable continuous wave (CW) laser. (b) Thermally tuning the resonance wavelength of the micro-resonator. Optically tuning the resonance wavelength of the micro-resonator using adjusting (c) the carrier light, and (d) pump light power levels.

Researchers in [61,105,106,125] have used the scheme in Figure 15b to implement bandpass MPFs using microring resonators, microdisk resonators, and photonic crystal cavities. In particular, Zhang and Yao have taken an important step forward in the full integration of microwave photonic systems on a single silicon chip by demonstrating the first-ever on-silicon-chip frequency-tunable bandpass MPF [61], consisting of a high-speed PM, a thermally tunable high Q-factor microdisk resonator (MDR), and a high-speed PD, as shown in Figure 17a,b. The high-speed PM has a traveling wave structure with a lateral PN junction in the rib waveguide and works on the reverse bias regime based on the free-carrier plasma dispersion effect in silicon, providing a 3-dB modulation bandwidth of 20.85 GHz. The high-speed PIN PD is realized by doping the silicon waveguide with germanium. Under a reverse bias voltage of 7.5 V, the PD has a 3-dB bandwidth of 15.69 GHz. MDR is at the heart of the system, which has a radius of 10  $\mu\text{m}$ . To increase the Q-factor, authors have designed specifically the MDR to incorporate an additional slab waveguide of 90-nm thickness to wrap the disk and the bus waveguide, in order to decrease the scattering loss of the propagating optical field due to the disk sidewall roughness [61]. MDR has a Q-factor of around  $85 \times 10^3$ , bandwidth of 1.93GHz and a rejection ratio of 5.8 dB. MDR is also designed to be thermally tunable by placing a metallic micro-heater on top of the disk. Figure 17c shows the measured frequency response of the implemented MPF with a center frequency of 5.84 GHz, with an electrical DC power of 0.33 mW applied to the micro-heater. The implemented MPF exhibits a 3-dB bandwidth of 1.93 GHz, which is equal to that of the notch resonance of the MDR, and a rejection ratio of 15 dB. Figure 17d shows the frequency responses of the MPF with the central frequency tuned from 3 to 10 GHz (tuning range of 7 GHz) when a tunable DC voltage is applied to the micro-heater.

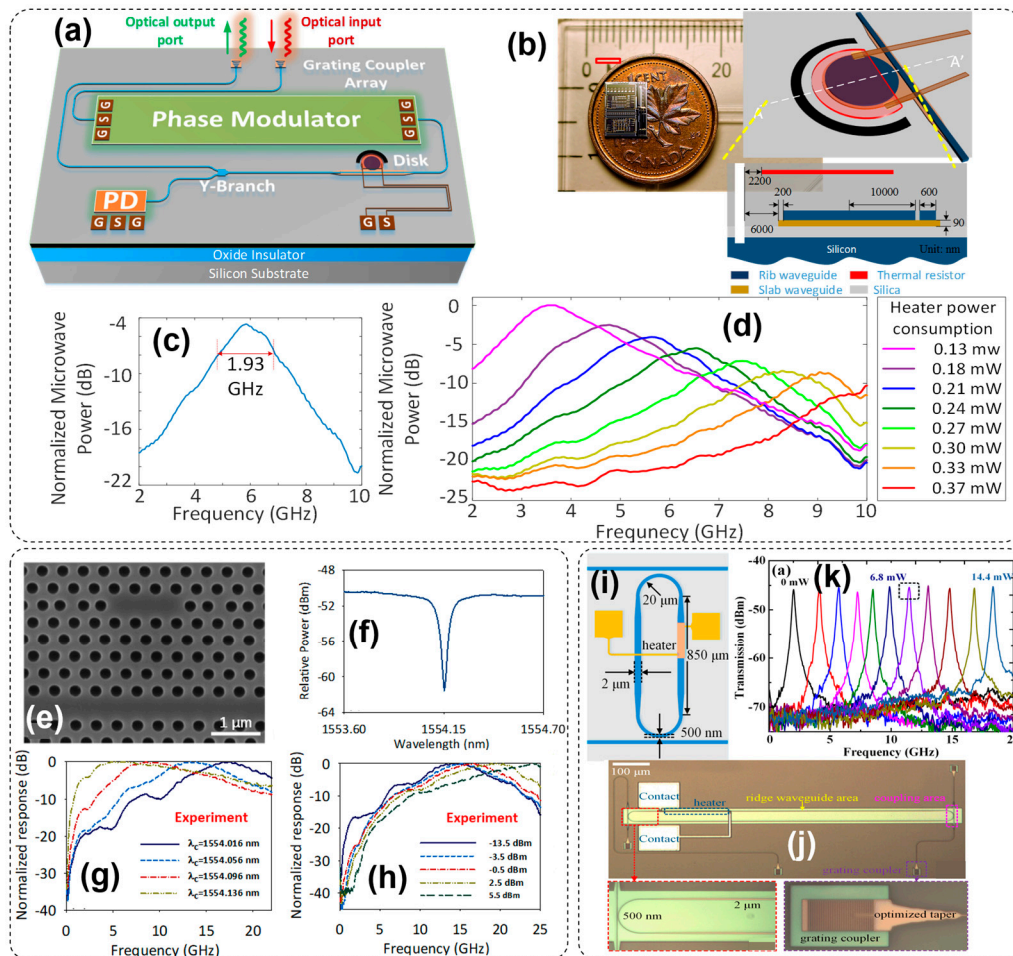


**Figure 17.** Implemented bandpass MPFs based on silicon micro-resonators. (a–d) On-chip integrated MPF based on microdisk resonator (MDR) reported in [61]: (a) perspective view of the proposed MPF, (b) image of the fabricated silicon photonic chip, schematic view of the thermally tunable MDR, cross-sectional view of the MDR, (c) experimental results of MPF and (d) measured frequency responses tuning from 3 to 10 GHz. Courtesy of and adapted from Jianping Yao [61]. (e–h) Ultracompact bandpass MPF based on a PhC microcavity reported in [105]: (e) SEM image, and (f) transmission spectrum of the fabricated silicon PhC microcavity, measured MPF responses at (g) different optical carrier wavelengths and (h) different optical carrier power levels. Courtesy of and adapted from Jian Wang [105]. (i–k) Ultranarrow bandpass MPF reported in [106]: (i) layout of the used ultra-high-Q MRR, (j) image of the fabricated MRR and (k) experimental results of tunable bandpass MPF. Courtesy of and adapted from Yuan Yu [106].

Another example of a bandpass IMWP, with all-optical tunability, was proposed in [105], showing an ultracompact, with around  $15 \mu\text{m}^2$  area, MPF based on a silicon photonic crystal (PhC) microcavity, as depicted in Figure 17e. Electron beam lithography (EBL, Vistec EBPG 5000 plus) and inductively coupled plasma (ICP) etching are used to define the pattern of the PhC microcavity on an SOI wafer. The lattice constant is  $420 \text{ nm}$  and the hole radius is  $126 \text{ nm}$ . Figure 17f shows the measured transmission spectrum of the fabricated PhC microcavity. The measured Q-factor of the cavity is around  $20 \times 10^3$  and the 3-dB bandwidth of the notch resonance is about  $9.5 \text{ GHz}$ . The optical carrier wavelength is located on the left side of the notch resonant wavelength of the PhC microcavity. Figure 17g shows the measured tunable MPF responses at different optical carrier wavelengths at a fixed and very low optical carrier power level, employing the tuning mechanism shown in Figure 16a. The full width at half maximum (FWHM) of the MPF is around  $9.5 \text{ GHz}$  and a tuning range from  $4.5$  to  $18.0 \text{ GHz}$  is obtained. They also optically tune the MPF responses at different optical carrier

power levels (see Figure 16c), where the its carrier wavelength is fixed, as illustrated in Figure 17h. When the optical carrier power increases from  $-13.5$  dBm to  $5.5$  dBm, the central frequency of the MPF is changed from  $13.9$  to  $24$  GHz. The notch resonant wavelength of the PhC microcavity red shifts as the optical carrier power increases. In addition, authors also study a second case where the optical carrier wavelength is located on the right side of the notch resonant wavelength of the PhC microcavity and observe an interesting bistable microwave response by increasing the carrier power.

As can be extrapolated from two examples above, one of the challenges of the most IMPFs using silicon micro-resonators is the poor resolution, i.e., high FWHM bandwidth, of above gigahertz, which is mainly restrained by the relative low Q-factor ( $\sim 10^4$  or  $10^5$ ) of silicon resonators. Another promising proposal featuring an ultra-narrowband bandpass filter with a wide frequency-tunability was presented in [106]. Qiu et al. have designed a new MRR, see Figure 17i, which exhibits an ultra-high Q-factor of  $1.14 \times 10^6$ . In this design, all the parameters affecting the Q-factor are well-optimized, including the perimeter, ring waveguide involving two half-rings and two race-tracks and the gap between the bus waveguide and the half-ring. Figure 17j shows the fabricated SOI MRR with a half-ring radius of  $20 \mu\text{m}$  and the width of half-ring and the race-track are set as  $500 \text{ nm}$  and  $2 \mu\text{m}$ , respectively. The race-track length is designed as  $850 \mu\text{m}$ , the length of linear taper connects the half-ring and the race-track is designed as  $50 \mu\text{m}$ . An ultra-narrowband MPF is achieved using this microresonator with a FWHM bandwidth and the rejection ratio of  $170 \text{ MHz}$  and  $26.5 \text{ dB}$ , respectively, as depicted in Figure 17k. A micro-heater on top of the MRR is used to tune the central frequency of the MPF from  $2.0 \text{ GHz}$  to  $18.4 \text{ GHz}$  with electrical power varied from  $0$  to  $14.4 \text{ mW}$ .

As important as bandpass MPFs, notch MPFs with high peak rejection are also highly desired in practical microwave applications. Most of recently reported notch filters uses the scheme shown in Figure 15c. For instance, the work reported in [107] uses a microdisk resonator (MDR) with a radius of  $10 \mu\text{m}$  and a Q-factor of  $107 \times 10^3$  to obtain a compact MPF with a 3-dB bandwidth of about  $2 \text{ GHz}$ , a rejection ratio of about  $40 \text{ dB}$ , and a frequency tuning range larger than  $12 \text{ GHz}$ . A tunable laser with a tuning resolution of  $1 \text{ pm}$  is used for frequency-tuning of the MPF (using the tuning mechanism depicted in Figure 16a). An all-optical frequency-tuning version of this filter, incorporating a MRR shown in Figure 18a, has also been reported in [108], in which the central frequency of the MPF can be flexibly tuned by changing a pump light power (see Figure 16d). Figure 18b shows the measured optical transmission spectrum of the MRR with a pump light, located at an immediate adjust notch resonance frequency, off and on. When the pump is on a red shift of the notch resonant wavelength is observed. In this work, the optical carrier wavelength is located on the both left and right sides of the notch resonance of the MRR and the effect of the pump light power on the resultant notch MPF is studied in both cases. propagating in both forward or backward directions respect to the carrier light. As an example, Figure 18c shows the results of the case where the optical carrier located at the left side of the notch resonance of the MRR (Case 1), the central frequency of the notch MPF is tuned from  $15.64$  to  $8.79 \text{ GHz}$ . For the Case 2 in which the optical carrier located at the right side of the notch resonance of the MRR, the central frequency of the notch MPF is tuned from  $5.27$  to  $12.47 \text{ GHz}$ , as depicted in Figure 18d. A detailed theoretical model is also established to explain the principle operation of the proposed all-optical tunable MPF in this research.

A more complex nonlinear tuning design has also been recently presented in [109] using an opto-mechanical MRR. The nonlinear opto-mechanical effect is induced by the opto-mechanical interaction between a pump light and a free-hanging MRR. As the gradient of the optical field is significantly enhanced in the MRR, the optical force pushing down the hanging section of the MRR could be amplified by several orders of magnitude. With injecting resonant pump light with milliwatt power level, the generated optical gradient force between the MRR and the underneath substrate could effectively cause nanometer or even micrometer deformation of the free-hanging ring, which would change the effective optical path of the MRR. Additionally, the thermo-optic effect also plays an important role to induce resonance red-shift which helps for reducing the pump power.

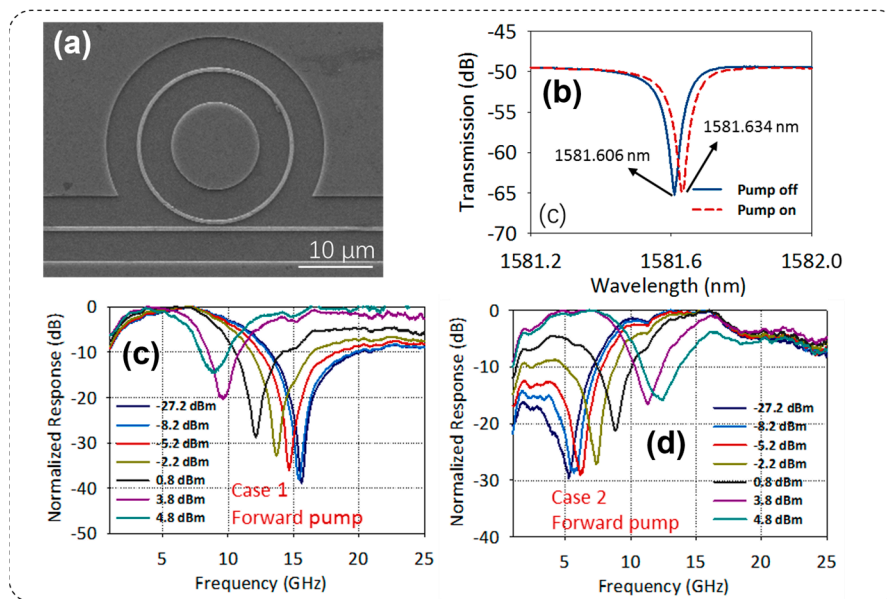


**Figure 18.** Implemented all-optical tunable notch MPF proposed in [108]: (a) SEM image and (b) measured transmission spectrum of the fabricated MRR with the pump light off and on, (c,d) measured microwave responses of the tunable MPF under different pump powers. Courtesy of and adapted from Jian Wang [108].

Using conventional OSSB modulation technologies to realize the notch MPF (Figure 15c), it is very difficult to realize high rejection ratio microwave filter beyond 50 dB, due to the relative low Q-factor of Silicon micro-resonators. In another approach [49], Long and Wang explore and implement an effective approach, based on an MPF design previously demonstrated in silicon nitride platform [126], to achieve an ultra-high peak rejection notch MPF using a  $\sim 16 \times 10^3$  Q-factor silicon MRR, the same micro-ring used in [108]. They successfully achieve a notch MPF with a tunable rejection ratio, reaching to an ultra-high peak rejection beyond 60 dB. Figure 19a summarizes the operation principle of the proposed notch MPF. An optical carrier is modulated by an RF signal with a conventional phase modulation technique. The modulated signal is then sent to a tunable optical bandpass filter (OBPF) and the USB signal is attenuated with control. The output field is next applied to the MRR, whose notch resonant wavelength is now aligned with that of the LSB signal, thus filtering the LSB signal. Since the rejection ratio of the MRR is not very high, the amplitude of the residual LSB signal could be equal to the USB signal. Therefore, owing to the equal amplitude and  $\pi$  phase difference of the USB and LSB, the signal power at the modulated frequency will be cancelled after detection by the PD. Figure 19b shows an SEM image of the used MRR and Figure 19c,d show the measured optical spectra after the OBPF and the corresponding MPF responses for two cases with rejection ratios of about 30 and 61.5 dB, respectively. They also show that the MPF can operate over a large tunable frequency range (12.4 to 30.6 GHz), keeping the ultra-high peak rejection property. To reduce the size, the same group also uses the silicon PhC nanocavity shown in Figure 17e in this MPF scheme and yet obtains a rejection ratio over 60 dB over a frequency range from 12.9 to 32.3 GHz [110].

More complex and elaborated MPF designs, involving more than one micro-resonators and incorporating MZIs, have also been recently presented [114–116,127]. For example, Minasian's group at the University of Sydney have demonstrated a tunable passband MPF based on an integrated optical double notch filter using a cascaded pair of non-identical MRRs (Figure 20a), in conjunction with optical phase modulation [114]. This approach attempts to address the non-zero phase issue of micro-resonators outside their resonance wavelengths. The principle operation of the proposed approach is shown in Figure 20b, where two MRR notch resonances are located on each side of the optical carrier to effectively cancel the additional phase introduced by each filter outside the

notch regions. Figure 20c depicts the experimental results of the implemented MPF, featuring a shape-invariant filter over the tuning range of 6–17 GHz.

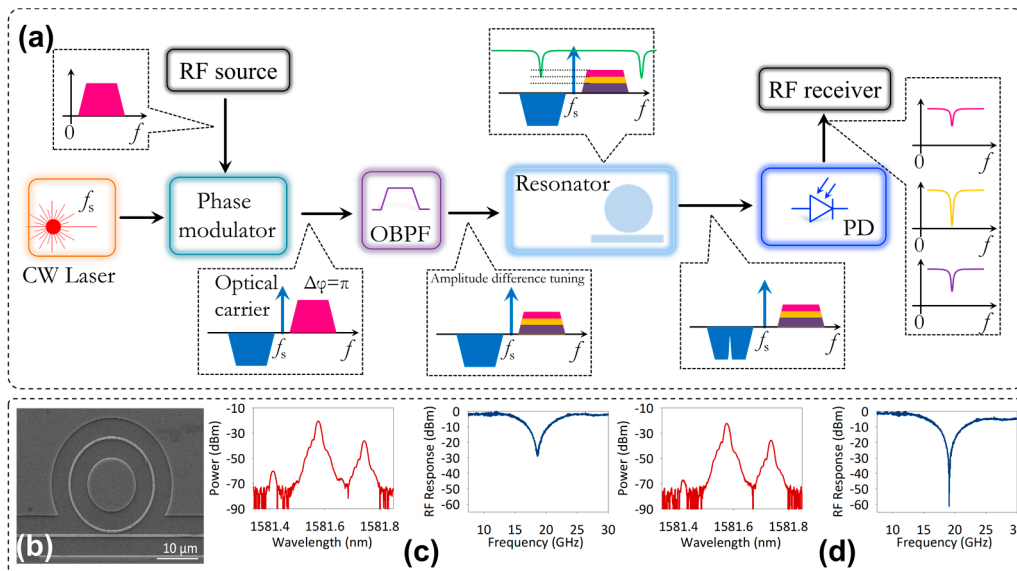


**Figure 19.** (a) Schematic illustration of the notch MPF with rejection ratio tunability proposed in [49], (b) SEM image of the silicon MRR, (c,d) Optical spectra after the tunable optical bandpass filter (OBPF) (dashed lines) and the corresponding MPF responses. Courtesy of and adapted from Jian Wang [49].

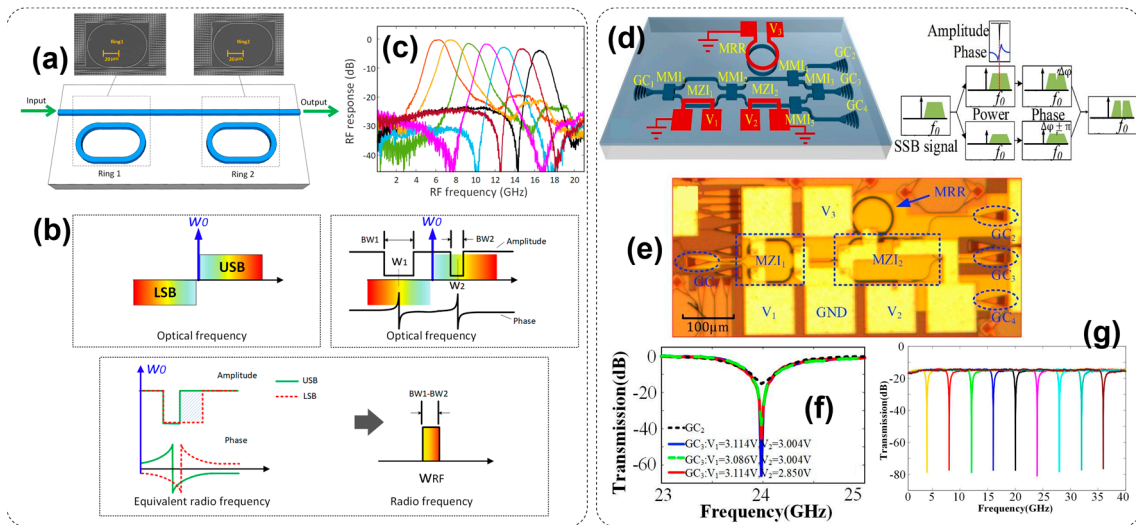


**Figure 20.** (a,b) Bandpass MPF based optical double notch filter reported in [114]: (a) Schematic diagram of the optical double notch filter, (b) operation principle of the proposed MPF, and (c) measured RF responses. Courtesy of and adapted from Xiaoke Yi [114]. (d–g) Ultrahigh peak rejection notch MPF proposed in [115]: (d) The structure and concept of the proposed MPF, (e) optical micrograph of the fabricated device, and (f,g) experimental results. Courtesy of and adapted from Yuan Yu [115].

In another elaborated design, Liu et al. from Huazhong University of Science and Technology, proposed a novel widely tunable MPF using an under-coupled MRR assisted by two cascaded tunable MZIs [115], shown in Figure 20d,e. Three heaters with voltages of  $V_1$ ,  $V_2$ , and  $V_3$  are designed on the lower arms of  $MZI_1$  and  $MZI_2$  (to control the amplitude balance and phase difference in MZIs) and the MRR (to control the center-frequency of the MPF), respectively. In short, the OSSB is split into the two arms of  $MZI_1$  by a coupler, and a phase difference of  $\phi_{MZI1}$  is obtained by tuning  $V_1$ . Therefore, signals with different amplitudes in the two arms of  $MZI_2$  are available due to the

interference induced by  $\phi_{MZI1}$ . After being processed by the MRR, the amplitude and the phase of the sideband in the upper arm at  $f_0$ , which corresponds to the resonant frequency of the MRR, will be changed by the MRR. Then,  $V_1$  and  $V_2$  are adjusted to equalize the amplitudes and obtain a  $\pi$  phase difference between the two sidebands in the two arms of  $MZI_2$  at  $f_0$ . Hence, destructive interference at the output of the output coupler is realized. Therefore, a MPF with ultrahigh peak rejection is implemented. In the experimental demonstration, they show a notch MPF with remarkable figure of merits, i.e., an ultrahigh peak rejection exceeding 60 dB, a *FWHM* bandwidth of 780 MHz, and a frequency tuning range of 0–40 GHz.

Finally, a few works have exploited nonlinear effects in silicon waveguides to implement a microwave filter response. For instance, Casas-Bedoya et al. in [118] demonstrated a narrowband notch MPF with a peak rejection 48-dB, 98-MHz linewidth, and 6-GHz frequency tuning based on the SBS nonlinear effect in a silicon nanowire. Figure 21a summarizes the operation principle of the narrowband MPF created by SBS. This technique employs the heterodyne photodetection to generate two RF mixing products between an optical carrier and two upper and lower sidebands [118]. These two mixing products interfere with each other. Nevertheless, destructive interference takes place only at the frequency where the sidebands have the equal amplitude and  $\pi$  phase difference. This amplitude/phase relationship between the upper and lower sidebands is achieved through SBS ( $\Omega_{SBSGain}$ ) on one of the sidebands. Therefore, the RF mixing products interfere destructively in the SBS bandwidth range, resulting in a narrowband microwave notch response. The center frequency of the notch filter can be tuned by varying the location of the SBS resonance, i.e., tuning the SBS pump wavelength. The silicon nanowire with a 1.25 cm length and a 220 by 480 nm cross-section was supported by a silica pillar of 50 nm width. The experimental setup and results of the notch MPF based on SBS are depicted in Figure 21b,d. Despite a low obtained SBS gain in this experiment,  $\Omega_{SBSGain} = 0.98$  dB, this scheme produces a high-suppression, greater than 48 dB, notch response. The center frequency of the notch in the RF domain can also be tuned by adjusting the wavelength of the SBS pump, as shown in Figure 21d.

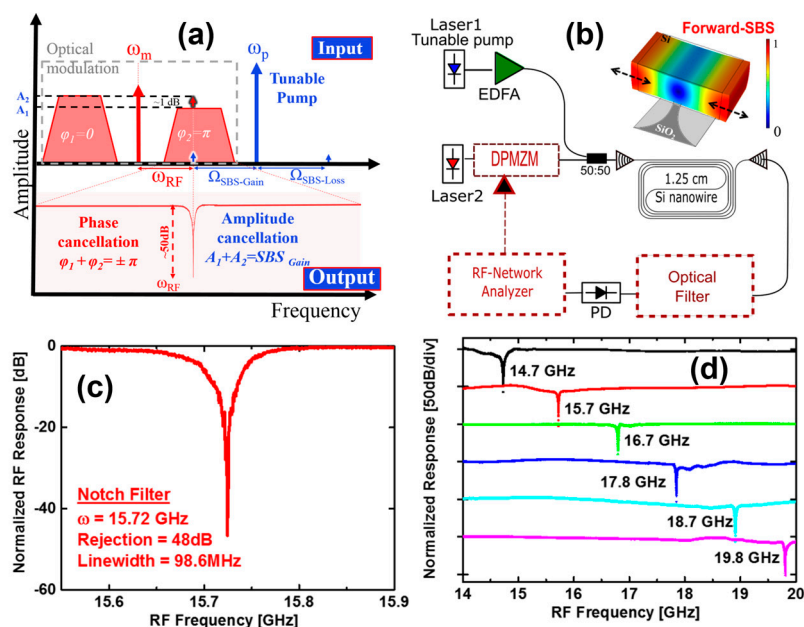


**Figure 21.** (a) Working principle of the MPF created by SBS in [118], (b) setup of the notch filter experiment, (c,d) Measured notch MPF responses. Courtesy of and adapted from Alvaro Casas-Bedoya [118].

## 7. Arbitrary Waveform Generation

Arbitrary waveform generation (AWG) is crucial to many RF tests, measurements and applications, including ultrawide-bandwidth wireless communications, and radar systems [3,14,40,74,128]. AWG is performed in electronic systems traditionally by oscillators based on two terminal devices (IMPATT, Gunn, quartz crystal, dielectric resonator) or three terminal devices (transistors) [3,14,40,74,128]. These approaches perform well in the 4.0 to 8.0 GHz (IEEE C-band for RF bands) and below frequency applications. However, for some emerging applications such as radars and satellite communication, this traditional method fails to produce satisfactory results [14,128,129]. Recent state-of-the-art electronic AWG systems are typically designed based on a digital synthesis approach followed by digital-to-analog conversion (DAC), providing greater frequency performance in the tens of GHz regime [130]. With the rapid development of microwave technologies, new applications require the use of shorter and shorter wavelengths (higher frequencies) and therefore, while continually improving, the electronic AWG methods are inherently limited and typically, there is a bandwidth-SNR tradeoff, i.e., the signal quality deteriorates significantly with the increase of working frequency. MWP has provided various high-bandwidth and efficient solutions for AWG by optical techniques, which are otherwise difficult to obtain by electronic means. These include direct space-to-time mapping [131], spectral shaping and wavelength-to-time mapping (SS-WTT) [132–134] and temporal pulse shaping [26,135], for generation of ultra-broad bandwidth RF waves with arbitrary and reconfigurable phase and amplitude or generation of extremely stable and pure microwave carriers. In this section, we review recent work on integrated MWP approaches for AWG and stable carrier generation using optoelectronic oscillators (OEO).

Perhaps SS-WTT is the best-known AWG approach and has received a great deal of attention due to its flexibility and simplicity [14,134]. The operation principle of the SS-WTT mapping technique is depicted in Figure 22. A typical SS-WTT mapping system comprises an ultra-short optical pulsed source, an optical spectral shaper, a dispersive medium, and a high-speed PD. An ultrashort optical pulse, generated from a mode-locked laser, is first spectrally tailored by an optical spectral shaper, which typically operates as a spectral amplitude filter. Then, the spectrum-shaped optical pulse is directed to a dispersive element, having a linear group delay (quadratic phase response) as a function of frequency with a slope of  $\dot{\phi}$ , to perform linear WTT mapping. At the output of the PD, a microwave waveform with a temporal shape identical to that of the shaped optical spectrum is generated. A key device for the generation of an arbitrary waveform in the SS-WTT system is therefore the spectral shaper that is designed to exhibit an amplitude spectral response with a shape corresponding to a scaled version of the temporal microwave waveform to be generated.

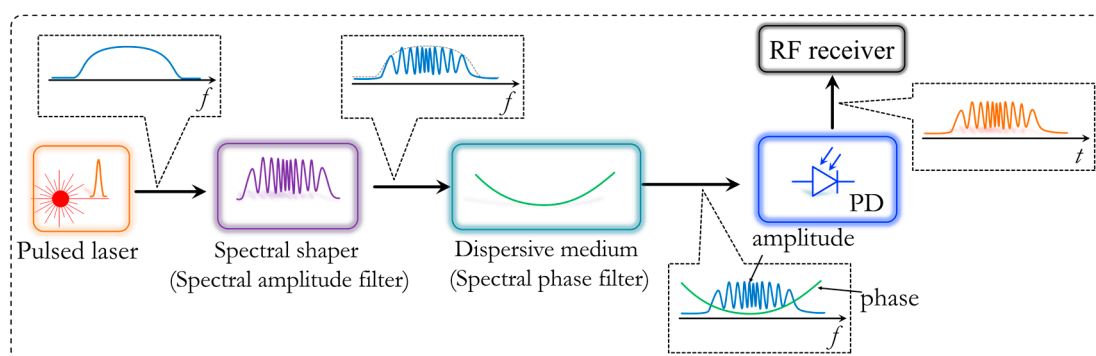


**Figure 22.** Schematic of an AWG system based on spectral shaping and wavelength-to-time mapping (SS-WTT) mapping technique.

Several on-silicon-chip spectral shapers have been proposed recently to generate various shapes of microwave waveforms [22,26,40,136–138]. Among them, linearly chirped microwave waveforms (LCMW) are of particular interest due to their range of applications in instrumentation, imaging,

and communications [139]. For example, they can be compressed to increase the detection distance and improve the measurement resolution for radar systems. Important characteristics of chirped RF waveforms include the central frequency ( $f_{RF}$ ), amount of RF chirp, and time bandwidth product (TBWP) (a larger TBWP allows for a higher compression ratio) [138]. For LCMW generation, the optical spectral shaper should exhibit a spectral amplitude response with an increasing or decreasing FSR. Several groups have actively investigated the implementation of spectral shapers on silicon chips. For instant, in recent years, Zhang and Yao have designed and reported three optical spectral shapers based on silicon photonics [22,136,137,140]. The first spectral shaper consists of multiple cascaded MRRs with largely different radii, as shown in Figure 23a. The spectral shaper has an MZI structure which incorporates multiple cascaded MRRs. Each MRR will selectively transfer the portion of the input optical power corresponding to its resonance wavelength from the through-port waveguide to the drop-port waveguide. The different colors of the rings depicted in Figure 23a show that each ring has a different radius and, therefore, a different resonant wavelength. By attentively designing the ring radii, reflection peaks with a linearly increasing FSR can be obtained at the reflection port. Figure 23b demonstrates the spectral response at the reflection port of an on-silicon-chip spectral shaper involving five MRRs. Figure 23c shows the experimentally generated LCMW in the SS-WTT mapping system, and Figure 23d illustrates the spectrogram of the generated LCMW, showing the temporal energy distribution of the microwave frequency components. The generated LCMW has a bandwidth of 15.5 GHz, a chirp rate of 17.2 GHz/ns, and a TBWP of 18.7. For practical applications, however, an LCMW with a much greater TBWP is required in order to enable large pulse compression. The second spectral shaper is then designed to have a greater TBWP [22,137].

Figure 23e illustrates the layout of the spectral shaper, which consists of an MZI structure incorporating two identical linearly chirped Bragg gratings (LCBGs) with opposite chirp rates in its arms. An input light beam is split by a Y-branch into two beams to propagate through the upper and lower LCBGs, which are realized by introducing periodic sidewall corrugations on the slab. Different wavelengths of the light spectrum are reflected from different positions in the LCBGs. The reflected light beams are then collected by the second and the third Y-branches, and recombined at the fourth Y-branch. Due to the interference effect, the spectral shaper exhibits a spectral response with a wavelength-dependent FSR. The center frequency of the generated LCMW can be tuned using an offset waveguide inserted in the lower arm of the spectral shaper to adjust the length difference between the two arms. Therefore, the spectral response of the spectral shaper can be adjusted to have a symmetrical, a uniformly decreasing or increasing FSR by appropriately designing the LCBGs and selecting the right length of the offset waveguide. Figure 23f shows the spectral response of a fabricated spectral shaper with a zero length of the offset waveguide, which leads to a spectral response with a symmetrical, and linearly increasing FSR on both sides. Figure 23g shows the spectral response of another fabricated on-chip spectral shaper with the offset waveguide length equal to the length of the LCBG, building up a spectral response with a linearly decreasing FSR. By incorporating the spectral shaper with the offset waveguide length of zero into an SS-WTT mapping system, an LCMW with a pulse duration of around 10.90 ns and a symmetrical chirp is generated, as shown in Figure 23h. The central frequency of the generated chirped microwave waveform is 1.2 GHz and the linearly increasing instantaneous frequency is 5.4 GHz/ns on the right side of the center, while that is  $-4.9$  GHz/ns on the left side of the center. The TBWP of around 359.7 is estimated for the generated LCMW. As another example, a spectral shaper with an offset waveguide length equal to the length of the LCBG is incorporated into the SS-WTT mapping system and an LCMW with a linearly increasing chirp is generated, as shown in Figure 23i. The generated LCMW has a pulse duration of around 20.5 ns and the center frequency of 15.8 GHz with a positive chirp rate of 1.54 GHz/ns. The TBWP is estimated to be around 615.

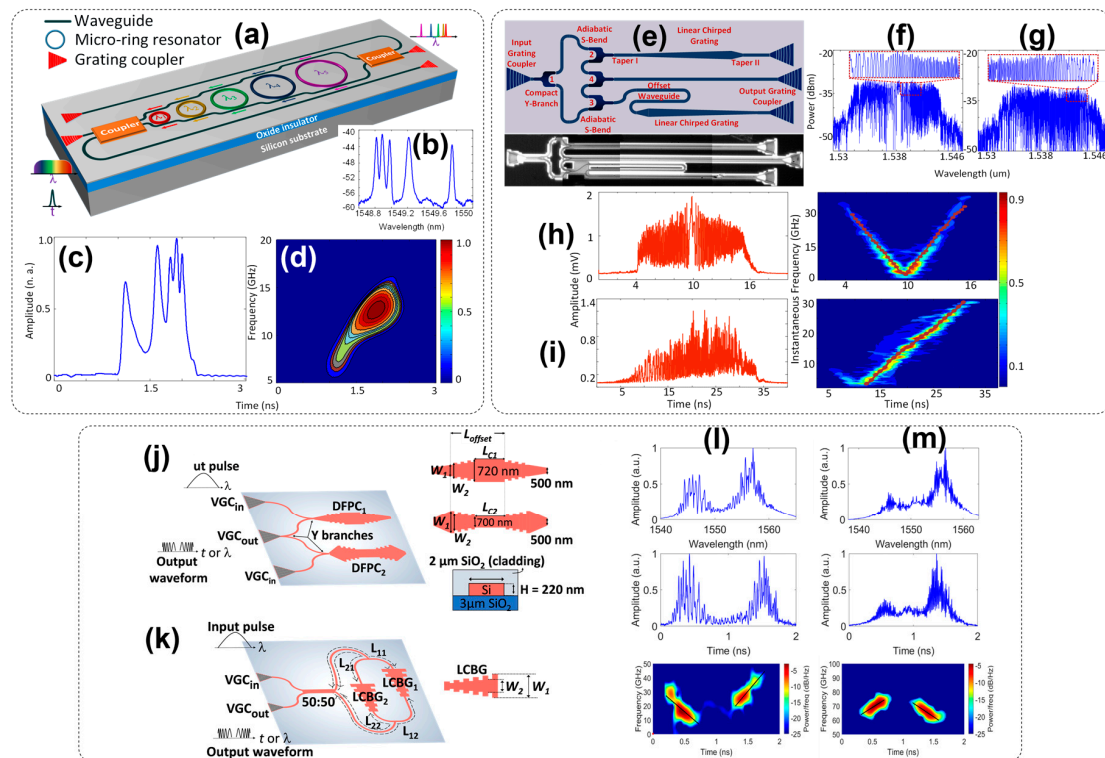


**Figure 23.** Recently implemented on-silicon-chip spectral shapers. (a–d) Spectral shaper consisting of five MRRs reported in [22,140]: (a) perspective view of the proposed spectral shaper; (b) measured spectral response of the spectral shaper; (c) generated linearly chirped microwave waveforms (LCMW) and (d) its spectrogram. Courtesy of and adapted from Jianping Yao [22,140]. (e–i) Spectral shaper incorporating two linearly chirped Bragg gratings (LCBGs) proposed in [22,137]: (e) Schematic layout and image of the fabricated on-chip spectral shaper; (f,g) Measured spectral response of the spectral shaper when the offset waveguide length is equal to (f) zero, and (g) the length of the LCBG; (h,i) Experimental results of on-chip spectral shaper corresponding to (f,g), respectively. Courtesy of and adapted from Jianping Yao [22,137]. (j–m) Spectral shaper of generation of multiple chirped RF waveforms reported in [138]: (j,k) proposed spectral shapers based on (j) parallel distributed Fabry-Pérot cavities (DFPCs) and (k) an arrayed waveguide Sagnac interferometer (AWGSI) incorporating LCBGs; (l,m) Experimental results for simultaneous generation of two chirped RF waveforms using the spectral shapers based on (l) DFPCs and (m) AWGSI incorporating LCBGs: top figure shows the measure spectra, middle figure shows the temporal waveforms, and bottom figure shows the calculated spectrograms.

In this scheme, the center frequency of the generated LCMW can be tuned by adjusting the center wavelength of the input optical pulse. To obtain an additional degree of tunability, the same group has taken advantage of the plasma dispersion effect in silicon and realized an electrically tunable LCBG and therefore an electrically tunable spectral shaper in their third proposal [136]. In this proposal, they employ instead a Michelson interferometer structure incorporating two LCBGs in its arms in which a lateral PN junction is introduced to the LCBG waveguides. By controlling the bias voltages of the PN junctions, a continuous chirp-rate tuning of a generated LCMW is demonstrated. In the experimental results, first, a LCMW with a central frequency of around 0.8 GHz, a positive chirp rate of 2.96 GHz/ns, and negative chirp rate of -6.25 GHz/ns was demonstrated in a non-biased configuration. By applying different voltage values, a maximum chirp rate tuning of 0.41GHz/nm was achieved. The estimated TBWP is varying between 95 to 140 depending on the applied voltage configuration. Nevertheless, the key advantage of this design is indeed the ultrafast electrical tuning of the generated LCMW, i.e., in a scale of nanoseconds, due to the ultrafast plasma dispersion effect.

Optical spectral shapers, including the examples mentioned above, are typically designed to operate only over one wavelength band, therefore, they can only generate a single LCMW. On the other hand, generating multiple LCMWs simultaneously, i.e., that are wavelength-division-multiplexed (WDM), can enhance the functionality of instrumentation and imaging systems. In [40,138], Chen et al. showed how the parallelism of optics can be exploited to generate multiple LCMWs with different  $f_{RF}$  and chirp rate simultaneously using parallel distributed Fabry-Pérot cavities (DFPC), and multiple LCBGs incorporated in an arrayed waveguide Sagnac interferometer (AWGSI). As the first design, Figure 23j shows the spectral shaper scheme based on two parallel DFPCs. Two DFPC designs (DFPC1 and DFPC2) are used to obtain the spectral shaper with opposite variations in FSR (and correspondingly, opposite signs of chirp rate in the generated waveforms). The LCBGs that comprise the DFPCs are based on a constant grating period and a linear variation in the waveguide width. The cavity is created using an offset length given by  $L_{offset,i} = L_{ci} +$  the length of one grating ( $i = 1,2$ ), in this example  $L_{c1} = 300 \mu\text{m}$  and  $L_{c2} = 600 \mu\text{m}$ .

In the second design, a two-channel spectral shaper based on incorporating two LCBGs in an AWGSI is shown, see Figure 23k. LCBG $_i$  ( $i = 1,2$ ) has a path imbalance of  $\Delta L_i = L_{i1} - L_{i2}$  where  $L_{i1}$  and  $L_{i2}$  are the two path lengths from LCBG $_i$  to the 3dB coupler, where LCBGs are similar to those used in the DFPC. The proof-of-concept experimental results for these two designs are summarized in Figure 23l,m, confirming the simultaneous generation of two LCMWs with opposite chirp rate signs. The estimated TBWP for the generated waveforms from the DFPC and AWGSI spectral shapers are  $\sim 7$  and  $\sim 3$ , respectively. Higher TBWP values are expected using an optimized design for LCBGs with longer length and/or chirp values.

The same group has also reported results of a more complex AWG design involving a N-tap MPF [27]. They use the four-wave mixing (FWM) in a silicon nanowire to increase the number of taps in the MPF. Then, using a benchtop programmable optical spectral shaper, the tap weights and corresponding generated waveforms are tuned.

The main issue of the reported approaches based on SS-WTT mapping is that the other important component of the AWG setup, the dispersive medium, is off-chip. Highly dispersive media that can provide the needed dispersion coefficient for the WTT over the desired optical bandwidth have yet to be realized in a silicon platform, despite many efforts [141–143].

In another demonstration of optics-based electronic AWG, an on-chip pulse shaping technique is exploited to generate programmable RF bursts and continuous waveforms [135]. The principle of the proposed photonic AWG system is shown in Figure 24a. A femtosecond optical pulse is replicated, delayed, and recombined through an eight-channel pulse shaper, comprising eight MRR add-drop filters of different radii. Spectral components of the input pulse corresponding to different resonances of a replica generation MRR are selected by that same MRR from the input through-port to form a channel replica pulse. The eight replicated pulses undergo various tunable delays (whose delay spectrum is schematically shown in the inset of Figure 24a) and are separated in the time domain. The amplitude of each pulse replica can be controlled during the recombination process by mismatching the resonances of the recombination and generation MRRs in the same channel through the thermo-optic effect. The properly delayed and scaled pulse replicas are collected at the output port of the pulse shaper to form the desired output optical waveform. Finally, the envelope of the output optical waveform is detected by an off-chip PD, producing the target RF waveform. An optical image of the fabricated pulse shaper is shown in Figure 24b. By independent control of the amplitude and delay in the shaper, various RF waveforms with amplitude, frequency, and phase modulations were created in this approach, as shown in Figure 24c. In particular, a LCMW is generated with a frequency modulation from 30 to 50 GHz in Figure 24c, bottom left.

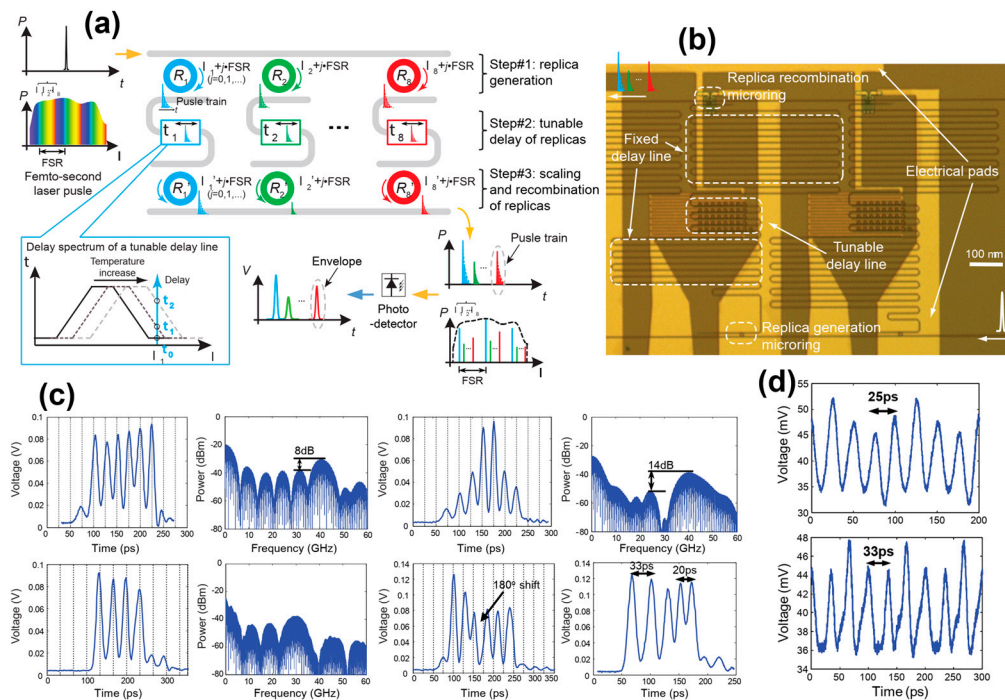


**Figure 24.** Pulse shaper consisting of 8 MRRs reported in [135]: (a) Operation principle of the proposed pulse shaper; (b) An optical image of a fabricated on-chip pulse shaper; (c) Demonstrated RF bursts and their spectra; (d) Single-tone continuous RF waveforms. Courtesy of and adapted from Minghao Qi and Andrew M. Weiner [135].

In the same design, as a secondary application, authors demonstrated the generation of continuous RF waveforms, using a 10-GHz optical frequency comb as a new light source. Figure 24d shows two examples for the generation of 30, and 40-GHz single-tone continuous RF waveforms. Nevertheless, the more effective approach for the generation of stable and pure continuous microwave signals have been reported in [144] and [145,146] and. In [144], a microwave signal generator has been proposed and experimentally demonstrated using a silicon microring modulator incorporating an embedded PN junction, as shown in Figure 25a. By properly designing the MRR, i.e., coupling conditions and operating wavelength, the DC component of the modulated light signal is trapped in the cavity whereas the high-order sideband components can exit the microring cavity and then generate microwave signals at multiplied frequencies in a PD. As an example, Figure 25b shows 8, 14, and 20 GHz microwave signals generated from 4, 7 and 10 GHz input microwave signals with higher than 22 dB harmonic suppression ratios. The ring modulator can also be cascaded or combined with a notch filter to achieve higher multiplication factors.

Finally, Yao’s group has used the same MPF integrated circuit explained in Section 6 [61] to realize an integrated optoelectronic oscillator (OEO) for generation of a frequency-tunable microwave signal [146]. With the forward injection of an optical wave into the chip, a bandpass MPF is achieved using the integrated circuit of PM, MDR, and PD. Nevertheless, if the output signal of the MPF is amplified and fed back to the input of the MPF, the MPF turns into an integrated OEO provided the gain is higher than the total losses of the cavity. The oscillation frequency of generated microwave signal is determined by the central frequency of the passband MPF. Therefore, by adjusting the electrical voltage applied to the micro-heater, located on top of the MDR (see Figure 25c), the central frequency of the passband MPF and, consequently, the oscillation frequency of the generated microwave signal is tuned. Additionally, the authors have also designed a second OEO whose MDR is controlled this time using a p-type doped silicon heater, as shown in Figure 25d. Both OEOs are able to generate a low phase noise microwave signal in the frequency range of 3 to 8 GHz. The measured phase noise of the generated microwave signal for both OEOs is around  $-80$  dBc/Hz at a 10-KHz

offset frequency. Experimental results of the OEO with the top-placed micro-heater and p-type doped silicon heater are depicted in Figure 25e,f, respectively. The OEO frequency is coarsely tuned from 2 to 8 GHz. Comparing the performances of the OEOs, the one with a micro-heater has noticeably better performance regarding frequency tuning range and phase noise. Because the doped silicon heater produces optical absorption losses in the MRD, the Q-factor of the MDR and, subsequently, the selectivity of the MPF is lower, thus the phase noise performance is degraded. For the implementation of an OEO, a high Q-factor MDR is more important, thus an OEO with a top-placed micro-heater is a better choice.

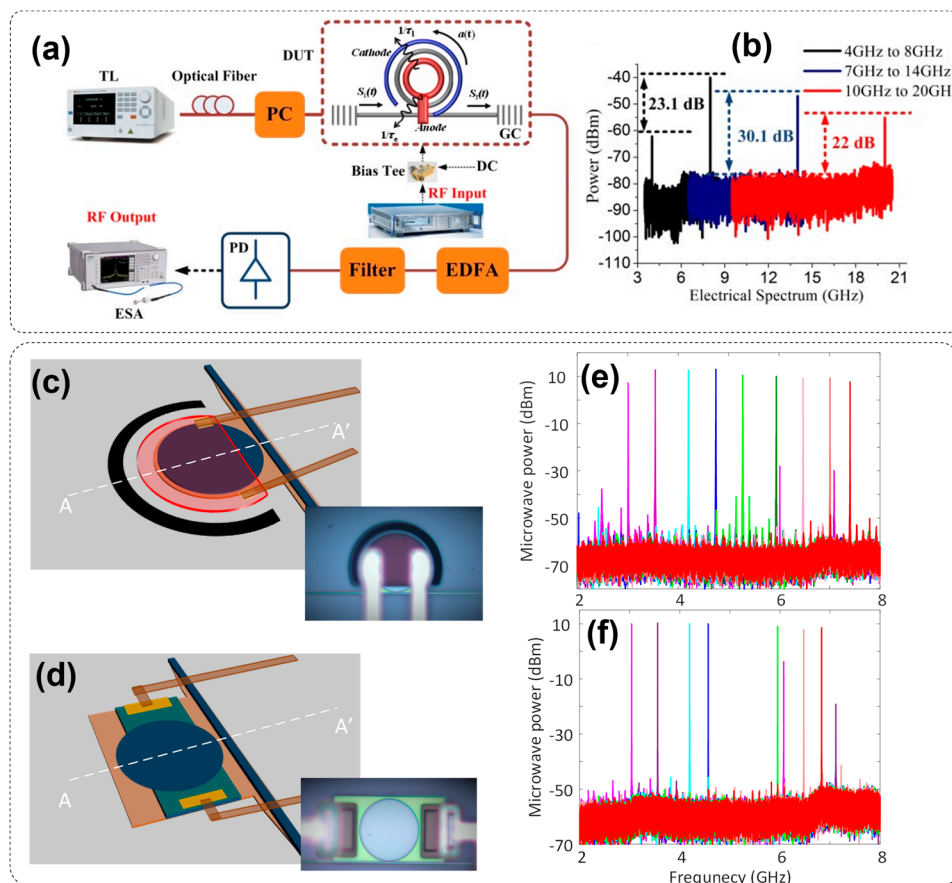


**Figure 25.** (a,b) generation of RF carrier based on a silicon microring modulator reported in [144]: (a) Schematic diagram of the microring modulator in the RF carrier generation setup; (b) measured electrical spectra for a 13 dBm input microwave signal. Courtesy of and adapted from Hui Yu [144]. (c–f) proposed silicon optoelectronic oscillators (OEO) reported in [146]: perspective view of the MDR (c) with a top-placed micro-heater and (d) with a p-type doped micro-heater; experimental result of the OEO with (e) a top-placed micro-heater and (f) a p-type doped silicon heater. Courtesy of and adapted from Jianping Yao [146].

### 8. Summary and Conclusion

We have provided a review of recent trends and advances on the implementation of key MWP circuits and functionalities on silicon platforms. We particularly focused on newly reported designs for microwave signal modulation, AWG, filtering, true-time delay, phase shifting, beam steering, and frequency measurement. Much progress has been achieved in the recent years concerning the development of microwave photonic systems on silicon platforms, and the field has reached a level of some maturity, as evidenced by the recent publications reviewed herein. Even though work has been reported on the use of thick silicon waveguides [104] and ultra-thin waveguides [95] to achieve lower propagation loss, it is important to note that most of the silicon based IMWP devices reported

to date are based on the standard 220 nm technology. This can be largely attributed to the adoption of the 220 nm technology by CMOS foundries as part of their multi-project wafer runs. Moreover, it is well understood that a 220 nm thick strip waveguide allows for ultra-compact circuits compared to thick or ultra-thin silicon waveguides. Compared to other waveguide platforms, InP platform inherently supports high performance active functionalities such as light generation, modulation, and detection, in addition to passive functionalities. Therefore, it provides all the tools needed for the full integration of MWP systems on a single chip. However, the main associated problems of this implementation are the larger size, higher loss, and increased fabrication cost, as well as the difficulty in achieving seamless integration with electronics. Dielectric materials (silica and silicon nitride waveguides) provide the lowest propagation losses, as low as 0.2dB/cm. However, they exhibit lower refractive index contrast that leads to large bending radius in the integrated circuits and hence, increases the chip size. Furthermore, these dielectric materials do not support high speed modulation and detection. Thus, it is not possible to implement high speed reconfigurable IMWP systems using such a dielectric platform. Moreover, silicon nitride waveguides suffer from very poor thermo-optic tuning efficiency ( $\sim 300 \text{ mW}/\pi$  phase shift).

The electro-optic (EO) and opto-electric (OE) conversions, large insertion losses and the use of optical amplifiers, to compensate the losses and for some systems to induce nonlinear effects, add noise to the MWP link, thereby degrading overall SNR and noise figure. Indeed, a central motivation of the idea of integration is that this would enable improving the system noise performance by reducing the losses and the need for optical amplification. One possible approach to further optimize the integrated MWP system's net loss is to minimize the propagation losses and the fiber-to-chip coupling losses. It is to be noted that full integration of the MWP systems into a single chip can eliminate the fiber-to-chip coupling losses and enhance significantly the system's noise performance. Further improvements in signal modulation and signal detection at the device level, including better linear performance of corresponding electronic circuits, is still required to improve the SNR at the EO and OE stages. Future progress in silicon-based MWP circuits will largely be determined by further developments in the critical active and passive components and the full integration of MWP systems on a single silicon chip. At the component level, there is a need to continue developing innovative designs for active and passive microwave photonic devices with improved figures of merit, consistently with present and future radio standards. At the system level, research efforts should focus on the integration of RF and active/passive photonic components in a single silicon platform. The promising demonstration by Yao [61] was a significant step forward in this direction.

**Funding:** J.A. and L.R.C. acknowledge financial support from NSERC. R.M. acknowledges the support of the Natural Sciences and Engineering Research Council of Canada (NSERC) through a Banting Postdoctoral Fellowship.

**Conflicts of Interest:** The authors declare no conflict of interest.

## References

1. Capmany, J.; Li, G.; Lim, C.; Yao, J. Microwave photonics: Current challenges towards widespread application. *Opt. Express* **2013**, *21*, 22862–22867. [[CrossRef](#)] [[PubMed](#)]
2. Minasian, R.A.; Chan, E.H.W.; Yi, X. Microwave photonic signal processing. *Opt. Express* **2013**, *21*, 22918–22936. [[CrossRef](#)] [[PubMed](#)]
3. Marpaung, D.; Roeloffzen, C.; Heideman, R.; Leinse, A.; Sales, S.R.; Capmany, J. Integrated microwave photonics. *Laser Photonics Rev.* **2013**, *7*, 506–538.
4. Yao, J. Microwave photonics. *J. Lightwave Technol.* **2009**, *27*, 314–335. [[CrossRef](#)]
5. Seed, A.J. Microwave photonic links. In Proceedings of the IEEE International Topical Meeting on Microwave Photonics (MWP), Ogunquit, ME, USA, 4–6 October 2004; IEEE: Piscataway, NJ, USA, 2004; pp. 16–19.
6. Capmany, J.; Sales, S.; Gasulla, I.; Mora, J.; Lloret, J.; Sancho, J. Innovative concepts in microwave photonics. *Waves* **2012**, *4*, 43–58.

7. Iezekiel, S.; Burla, M.; Klamkin, J.; Marpaung, D.; Capmany, J. RF engineering meets optoelectronics: Progress in integrated microwave photonics. *IEEE Microw. Mag.* **2015**, *16*, 28–45. [[CrossRef](#)]
8. Urick, V.J.; Williams, K.J.; McKinney, J.D. *Fundamentals of Microwave Photonics*; Wiley: Hoboken, NJ, USA, 2015.
9. Iezekiel, S. *Microwave Photonics: Devices and Applications*; John Wiley & Sons: Hoboken, NJ, USA, 2009.
10. Fong, T.K.; Sabido, D.; Kazovsky, L.G. Linewidth-insensitive coherent AM analog optical links using semiconductor lasers. *IEEE Photonics Technol. Lett.* **1993**, *5*, 469–471. [[CrossRef](#)]
11. Seeds, A.J. Microwave opto-electronics. In Proceedings of the EDMO, Leeds, UK, 25–26 November 1996; pp. 44–49.
12. Cai, B.; Seeds, A.J. Optical frequency modulation links: Theory and experiments. *IEEE Trans. Microw. Theory Tech.* **1997**, *45*, 505–511. [[CrossRef](#)]
13. Wang, C.; Yao, J. Fiber Bragg Gratings for Microwave Photonics Subsystems. *Opt. Express* **2013**, *21*, 22868–22884. [[CrossRef](#)]
14. Lin, B.; Pan, B.; Zheng, Z.; Li, M.; Tjin, S.C. A review of photonic microwave generation. In Proceedings of the IEEE Optoelectronics Global Conference (OGC), Shenzhen, China, 5–7 September 2016; pp. 1–3.
15. Reptin, F.; Le Helleye, P. Microwave Photonics solutions for military systems. In Proceedings of the International Topical Meeting on Microwave Photonics (MWP), Grenoble, France, 3–6 October 2006; pp. 1–3.
16. Alphones, A. Recent trends in optical microwave interaction. In Proceedings of the 3rd International Conference on Microwave and Millimeter Wave Technology, Beijing, China, 17–19 August 2002; pp. 38–45.
17. Iezekiel, S.; Elamaram, B.; Pollard, R.D. Trends in microwave photonic network analysers. In Proceedings of the IEE Colloquium on Opto-Electronic Interfacing at Microwave Frequencies, London, UK, 20 April 1999.
18. Capmany, J.; Mora, J.; Gasulla, I.; Sancho, J.; Lloret, J.; Sales, S. Microwave photonic signal processing. *J. Lightwave Technol.* **2013**, *31*, 571–586. [[CrossRef](#)]
19. Hosseinzadeh, N.; Jain, A.; Helkey, R.; Buckwalter, J.F. RF silicon photonics for wideband, high dynamic range microwave and millimeter-wave signal processing. In Proceedings of the IEEE 18th Topical Meeting on Silicon Monolithic Integrated Circuits in RF Systems (SiRF), Anaheim, CA, USA, 14–17 January 2018; pp. 41–44.
20. Yi, X.; Chew, S.X.; Song, S.; Nguyen, L.; Minasian, R. Integrated microwave photonics for wideband signal processing. *Photonics* **2017**, *4*, 46. [[CrossRef](#)]
21. Fandino, J.; Domenech, J.; Munoz, P.; Capmany, J. Integrated InP frequency discriminator for Phase-modulated microwave photonic links. *Opt. Express* **2013**, *21*, 3726–3736. [[CrossRef](#)] [[PubMed](#)]
22. Zhang, W.; Yao, J. Silicon-Based Integrated Microwave Photonics. *IEEE J. Quantum Electron.* **2016**, *52*, 1–12. [[CrossRef](#)]
23. Capmany, J.; Ortega, B.; Pastor, D. A tutorial on microwave photonic filters. *J. Lightwave Technol.* **2006**, *24*, 201–229. [[CrossRef](#)]
24. Capmany, J.; Pastor, D.; Martinez, A.; Ortega, B.; Sales, S. Microwave photonic filters with negative coefficients based on phase inversion in an electro-optic modulator. *Opt. Lett.* **2003**, *28*, 1415–1417. [[CrossRef](#)] [[PubMed](#)]
25. Hamidi, E.; Leaird, D.E.; Weiner, A.M. Tunable programmable microwave photonic filters based on an optical frequency comb. *IEEE Trans. Microw. Theory Tech.* **2010**, *58*, 3269–3278. [[CrossRef](#)]
26. Yang, T.; Wu, Z.; Liu, L.; Dong, J. Radio frequency arbitrary waveform generation using ultracompact cascaded silicon microdisk resonators. In Proceedings of the OptoElectronics and Communication Conference and Australian Conference on Optical Fibre Technology, Melbourne, Australia, 6–10 July 2014; pp. 81–83.
27. Adams, R.; Ashrafi, R.; Wang, J.; Dizaji, M.R.; Chen, L.R. RF-arbitrary waveform generation based on microwave photonic filtering. *IEEE Photonics J.* **2014**, *6*, 1–8. [[CrossRef](#)]
28. Mckenna, T.P.; Nanzer, J.A.; Clark, T.R. Photonic beamsteering of a millimeter-wave array with 10-Gb/s data transmission. *IEEE Photonics Technol. Lett.* **2014**, *26*, 1407–1410. [[CrossRef](#)]
29. Newberg, I.L. Optoelectronic Wide Bandwidth Photonic Beamsteering Phased Array. U.S. Patent No 5,051,754, 1991.
30. Hallstig, E.J.; Ohgren, J.; Allard, L.; Sjoqvist, L.J.; Engstroem, D.; Hard, S.; AAgren, D.; Junique, S.; Wang, Q.; Noharet, B. Retrocommunication utilizing electroabsorption modulators and nonmechanical beam steering. *Opt. Eng.* **2005**, *44*, 045001. [[CrossRef](#)]

31. Chew, S.X.; Nguyen, L.; Yi, X.; Song, S.; Li, L.; Bian, P.; Minasian, R. Distributed optical signal processing for microwave photonics subsystems. *Opt. Express* **2016**, *24*, 4730–4739. [[CrossRef](#)]
32. Adams, D.B.; Madsen, C.K. A Novel Broadband Photonic RF Phase Shifter. *J. Lightwave Technol.* **2008**, *26*, 2712–2717. [[CrossRef](#)]
33. Loayssa, A.; Lahoz, F.J. Broad-band RF photonic phase shifter based on stimulated Brillouin scattering and single-sideband modulation. *IEEE Photonics Technol. Lett.* **2006**, *18*, 208–210. [[CrossRef](#)]
34. Ehteshami, N.; Zhang, W.; Yao, J. Optically tunable full 360° microwave photonic phase shifter using three cascaded silicon-on-insulator microring resonators. *Opt. Commun.* **2016**, *373*, 53–58. [[CrossRef](#)]
35. Capmany, J.; Ortega, B.; Pastor, D.; Sales, S. Discrete-time optical processing of microwave signals. *J. Lightwave Technol.* **2005**, *23*, 702–723. [[CrossRef](#)]
36. Capmany, J.; Gasulla, I.; Perez, D. Microwave photonics: The programmable processor. *Nat. Photonics* **2016**, *10*, 6. [[CrossRef](#)]
37. Coldren, L.A. Photonic integrated circuits for microwave photonics. In Proceedings of the IEEE Topical Meeting on Microwave Photonics (MWP), Montreal, QC, Canada, 5–9 October 2010; pp. 1–4.
38. Gasulla, I.; Lloret, J.; Sancho, J.; Sales, S.; Capmany, J. Recent breakthroughs in microwave photonics. *IEEE Photonics J.* **2011**, *3*, 311–315. [[CrossRef](#)]
39. Perez, D.; Gasulla, I.; Capmany, J. Software-defined reconfigurable microwave photonics processor. *Opt. Express* **2015**, *23*, 14640–14654. [[CrossRef](#)] [[PubMed](#)]
40. Chen, L.R. Silicon photonics for microwave photonics applications. *J. Lightwave Technol.* **2017**, *35*, 824–835. [[CrossRef](#)]
41. Yao, J. Photonic integrated circuits for microwave photonics. In Proceedings of the IEEE Photonics Conference (IPC) Part II, Orlando, FL, USA, 1–5 October 2017; pp. 1–2.
42. Wang, J. Ultracompact microwave photonic signal processing using silicon nanophotonic devices. In Proceedings of the 14th International Conference on Optical Communications and Networks (ICOON), Nanjing, China, 3–5 July 2015; pp. 1–5.
43. Ng, W. Photonics for microwave systems and ultra-wideband signal processing. *Opt. Commun.* **2016**, *373*, 2–15. [[CrossRef](#)]
44. Bowers, J.E. Integrated microwave photonics. In Proceedings of the International Topical Meeting on Microwave Photonics (MWP), Paphos, Cyprus, 26–29 October 2015; pp. 1–4.
45. Ghelfi, P.; Laghezza, F.; Scotti, F.; Serafino, G.; Pinna, S.; Onori, D.; Lazzeri, E.; Bogoni, A. Photonics in radar systems: RF integration for state-of-the-art functionality. *IEEE Microw. Mag.* **2015**, *16*, 74–83. [[CrossRef](#)]
46. Fandino, J.S.; Munoz, P.; Domenech, D.; Capmany, J. A monolithic integrated photonic microwave filter. *Nat. Photonics* **2017**, *11*, 124. [[CrossRef](#)]
47. Norberg, E.J.; Guzzon, R.S.; Parker, J.S.; Johansson, L.A.; Coldren, L.A. Programmable photonic microwave filters monolithically integrated in InP-InGaAsP. *J. Lightwave Technol.* **2011**, *29*, 1611–1619. [[CrossRef](#)]
48. Burla, M.; Romero Cortes, L.; Li, M.; Wang, X.; Chrostowski, L.; Azana, J. Integrated waveguide Bragg gratings for microwave photonics signal processing. *Opt. Express* **2013**, *21*, 25120–25147. [[CrossRef](#)] [[PubMed](#)]
49. Long, Y.; Wang, J. Ultra-high peak rejection notch microwave photonic filter using a single silicon microring resonator. *Opt. Express* **2015**, *23*, 17739–17750. [[CrossRef](#)] [[PubMed](#)]
50. Serafino, G.; Porzi, C.; Velha, P.; Andriolli, N.; Ghelfi, P.; Bogoni, A. 40 dB-rejection sharp-edge integrated SOI phase-shifted bragg grating filter for microwave photonics. In Proceedings of the 42nd European Conference on Optical Communication (ECOC), Dusseldorf, Germany, 18–22 September 2016; pp. 1–3.
51. Mickelson, A. Silicon photonics for microwave photonics. In Proceedings of the 3rd International Conference on Microwave and Photonics (ICMAP), Dhanbad, India, 9–11 February 2018; pp. 1–2.
52. Roeloffzen, C.G.; Zhuang, L.; Taddei, C.; Leinse, A.; Heideman, R.G.; van Dijk, P.W.; Oldenbeuving, R.M.; Marpaung, D.; Burla, M.; Boller, K.-J. Silicon nitride microwave photonic circuits. *Opt. Express* **2013**, *21*, 22937–22961. [[CrossRef](#)]
53. Marpaung, D. On-chip photonic-assisted instantaneous microwave frequency measurement system. *IEEE Photonics Technol. Lett.* **2013**, *25*, 837–840. [[CrossRef](#)]
54. Burla, M.; Marpaung, D.; Zhuang, L.; Roeloffzen, C.; Khan, M.R.; Leinse, A.; Hoekman, M.; Heideman, R. On-chip CMOS compatible reconfigurable optical delay line with separate carrier tuning for microwave photonic signal processing. *Opt. Express* **2011**, *19*, 21475–21484. [[CrossRef](#)]

55. Marpaung, D.; Roeloffzen, C.; Leinse, A.; Hoekman, M. A photonic chip based frequency discriminator for a high performance microwave photonic link. *Opt. Express* **2010**, *18*, 27359–27370. [[CrossRef](#)]
56. Marpaung, D.; Morrison, B.; Pagani, M.; Pant, R.; Choi, D.; Luther-Davies, B.; Madden, S.J.; Eggleton, B.J. Low-power, chip-based stimulated Brillouin scattering microwave photonic filter with ultrahigh selectivity. *Optica* **2015**, *2*, 76–83. [[CrossRef](#)]
57. Pant, R.; Marpaung, D.; Kabakova, I.V.; Morrison, B.; Poulton, C.G.; Eggleton, B.J. On-chip stimulated Brillouin Scattering for microwave signal processing and generation. *Laser Photonics Rev.* **2014**, *8*, 653–666.
58. Pelusi, M.; Luan, F.; Vo, T.D.; Lamont, M.R.; Madden, S.J.; Bulla, D.A.; Choi, D.-Y.; Luther-Davies, B.; Eggleton, B.J. Photonic-chip-based radio-frequency spectrum analyser with terahertz bandwidth. *Nat. Photonics* **2009**, *3*, 139–143. [[CrossRef](#)]
59. Jalali, B.; Fathpour, S. Silicon photonics. *J. Lightwave Technol.* **2006**, *24*, 4600–4615. [[CrossRef](#)]
60. Soref, R. The past, present, and future of silicon photonics. *IEEE J. Sel. Top. Quantum Electron.* **2006**, *12*, 1678–1687. [[CrossRef](#)]
61. Zhang, W.; Yao, J. On-chip silicon photonic integrated frequency-tunable bandpass microwave photonic filter. *Opt. Lett.* **2018**, *43*, 3622–3625. [[CrossRef](#)]
62. Liu, A.Y.; Srinivasan, S.; Norman, J.; Gossard, A.C.; Bowers, J.E. Quantum dot lasers for silicon photonics. *Photonics Res.* **2015**, *3*, B1–B9. [[CrossRef](#)]
63. Otterstrom, N.T.; Behunin, R.O.; Kittlaus, E.A.; Wang, Z.; Rakich, P.T. A silicon Brillouin laser. *Science* **2018**, *360*, 1113–1116. [[CrossRef](#)] [[PubMed](#)]
64. Bowers, J.E.; Liu, A.Y. A comparison of four approaches to photonic integration. In Proceedings of the Optical Fiber Communication Conference (OFC), Los Angeles, CA, USA, 19–23 March 2017.
65. Chen, H.-W.; Fang, A.W.; Peters, J.D.; Wang, Z.; Bovington, J.; Liang, D.; Bowers, J.E. Integrated microwave photonic filter on a hybrid silicon platform. *IEEE Trans. Microw. Theory Tech.* **2010**, *58*, 3213–3219. [[CrossRef](#)]
66. Kim, J.-H.; Aghaeimeibodi, S.; Richardson, C.J.; Leavitt, R.P.; Englund, D.; Waks, E. Hybrid integration of solid-state quantum emitters on a silicon photonic chip. *Nano Lett.* **2017**, *17*, 7394–7400. [[CrossRef](#)]
67. Wang, Z.; Abbasi, A.; Dave, U.; De Groote, A.; Kumari, S.; Kunert, B.; Merckling, C.; Pantouvaki, M.; Shi, Y.; Tian, B.; et al. Novel light source integration approaches for silicon photonics. *Laser Photonics Rev.* **2017**, *11*, 1700063.
68. Moscoso-Mártir, A.; Merget, F.; Mueller, J.; Hauck, J.; Romero-Garcia, S.; Shen, B.; Lelarge, F.; Brenot, R.; Garreau, A.; Mentovich, E.; et al. Hybrid silicon photonics flip-chip laser integration with vertical self-alignment. In Proceedings of the Conference on Lasers and Electro-Optics Pacific Rim (CLEO-PR), Singapore, 31 July–4 August 2017; pp. 1–4.
69. Billah, M.B.; Blaicher, M.; Hoose, T.; Dietrich, P.I.; Marin-Palomo, P.; Lindenmann, N.; Nestic, A.; Hofmann, A.; Troppenz, U.; Moehrle, M.; et al. Hybrid integration of silicon photonics circuits and InP lasers by photonic wire bonding. *arXiv*, 2018; arXiv:1802.03454.
70. Gu, Z.; Amemiya, T.; Ishikawa, A.; Hiratani, T.; Suzuki, J.I.; Nishiyama, N.; Tanaka, T.; Arai, S. Optical transmission between III-V chips on Si using photonic wire bonding. *Opt. Express* **2015**, *23*, 22394–22403. [[CrossRef](#)]
71. Sun, G. Intersubband approach to silicon based lasers—Circumventing the indirect bandgap limitation. *Adv. Opt Photonics* **2011**, *3*, 53–87. [[CrossRef](#)]
72. Chen, S.; Li, W.; Wu, J.; Jiang, Q.; Tang, M.; Shutts, S.; Elliott, S.N.; Sobiesierski, A.; Seeds, A.J.; Ross, I.; et al. Electrically pumped continuous-wave III–V quantum dot lasers on silicon. *Nat. Photonics* **2016**, *10*, 307. [[CrossRef](#)]
73. Chen, M.; Yu, H.; Wang, J. Silicon photonics-based signal processing for microwave photonic frontends. In *Silicon Photonics III*; Springer: Berlin, Germany, 2016; pp. 317–347.
74. Wang, J.; Long, Y. Chip-Scale Microwave Photonic Signal Processing. In *Microwave Systems and Applications*; InTech: London, UK, 2017.
75. Lee, C.H. *Microwave Photonics*, 2nd ed.; CRC Press: Boca Raton, FL, USA, 2013; p. 496.
76. Li, M.; Zhu, N. Recent advances in microwave photonics. *Front. Optoelectron.* **2016**, *9*, 160–185. [[CrossRef](#)]
77. Zhu, W.; Gu, Y.; Fan, F.; Han, X.; Li, J.; Hu, J.; Wu, Z.; Zhao, M. Recent progress of research on microwave photonic signal transmission and processing. In Proceedings of the International Topical Meeting on Microwave Photonics (MWP), Beijing, China, 23–26 October 2017; pp. 1–4.

78. Zhuang, L.; Xie, Y.; Lowery, A.J. Photonics-enabled innovations in RF engineering. In Proceedings of the Australian Microwave Symposium (AMS), Brisbane, Australia, 6–7 February 2018; pp. 7–8.
79. Ortega, B.; Cruz, J.L.; Capmany, J.; Andres, M.V.; Pastor, D. Variable delay line for phased-array antenna based on a chirped fiber grating. *IEEE Trans. Microw. Theory Tech.* **2000**, *48*, 1352–1360. [[CrossRef](#)]
80. Tang, Z.; Pan, S.; Yao, J. A High resolution optical vector network analyzer based on a wideband and wavelength-tunable optical single-sideband modulator. *Opt. Express* **2012**, *20*, 6555–6560. [[CrossRef](#)] [[PubMed](#)]
81. Song, S.; Yi, X.; Chew, S.X.; Li, L.; Nguyen, L.; Zheng, R. Optical single-sideband modulation based on silicon-on-insulator coupled-resonator optical waveguides. *Opt. Eng.* **2015**, *55*, 031114. [[CrossRef](#)]
82. Qi, G.; Yao, J.; Seregelyi, J.; Paquet, S.; Belisle, C. Generation and distribution of a wide-band continuously tunable millimeter-wave signal with an optical external modulation technique. *IEEE Trans. Microw. Theory Tech.* **2005**, *53*, 3090–3097.
83. Long, Y.; Zhou, L.; Wang, J. Photonic-assisted microwave signal multiplication and modulation using a silicon Mach-Zehnder modulator. *Sci. Rep.* **2016**, *6*, 20215. [[CrossRef](#)]
84. Pan, S.; Yao, J. Provision of IR-UWB wireless and baseband wired services over a WDM-PON. *Opt. Express* **2011**, *19*, B209–B217. [[CrossRef](#)]
85. Xu, K.; Wu, X.; Sung, J.; Cheng, Z.; Chow, C.W.; Song, Q.H.; Tsang, H.K. Amplitude and phase modulation of UWB monocycle pulses on a silicon photonic chip. *IEEE Photonics Technol. Lett.* **2016**, *28*, 248–251.
86. Basu, A.; Koul, S.K. Theory and design of solid-state microwave phase shifters. *IETE J. Educ.* **2009**, *50*, 9–18. [[CrossRef](#)]
87. Burla, M.; Cortes, L.R.; Li, M.; Wang, X.; Chrostowski, L.; Azana, J. On-chip programmable ultra-wideband microwave photonic phase shifter and true time delay unit. *Opt. Lett.* **2014**, *39*, 6181–6184. [[CrossRef](#)] [[PubMed](#)]
88. Porzi, C.; Serafino, G.; Sans, M.; Falconi, F.; Sorianello, V.; Pinna, S.; Mitchell, J.; Romagnoli, M.; Bogoni, A.; Ghelfi, P. Photonic integrated microwave phase shifter up to the mm-wave band with fast response time in silicon-on-insulator technology. *J. Lightwave Technol.* **2018**, *36*, 4494–4500. [[CrossRef](#)]
89. Polo, V.; Vidal, B.; Corral, J.; Marti, J. Novel tunable photonic microwave filter based on laser arrays and NXN AWG-based delay lines. *J. Lightwave Technol.* **2003**, *15*, 584–586.
90. Mokhtari, A.; Jamshidi, K.; Preussler, S.; Zadok, A.; Schneider, T. Tunable microwave-photonic filter using frequency-to-time mapping-based delay lines. *Opt. Express* **2013**, *21*, 21702–21707. [[CrossRef](#)] [[PubMed](#)]
91. Moreira, R.L.; Garcia, J.; Li, W.; Bauters, J.; Barton, J.S.; Heck, M.J.; Bowers, J.E.; Blumenthal, D.J. Integrated ultra-low-loss 4-bit tunable delay for broadband phased array antenna applications. *IEEE Photonics Technol. Lett.* **2013**, *25*, 1165–1168. [[CrossRef](#)]
92. Minasian, R.A. Ultra-wideband and adaptive photonic signal processing of microwave signals. *IEEE J. Quantum Electron.* **2016**, *52*, 1–13. [[CrossRef](#)]
93. Zhang, W.; Yao, J. Electrically tunable silicon-based on-chip microdisk resonator for integrated microwave photonic applications. *APL Photonics* **2016**, *1*, 080801. [[CrossRef](#)]
94. Wang, J.; Ashrafi, R.; Adams, R.; Glesk, I.; Gasulla, I.; Capmany, J.; Chen, L.R. Subwavelength grating enabled on-chip ultra-compact optical true time delay line. *Sci. Rep.* **2016**, *6*, 30235. [[CrossRef](#)]
95. Wang, X.; Zhou, L.; Li, R.; Xie, J.; Lu, L.; Wu, K.; Chen, J. Continuously tunable ultra-thin silicon waveguide optical delay line. *Optica* **2017**, *4*, 507–515. [[CrossRef](#)]
96. Wang, G.; Dai, T.; Jiang, J.; Guo, X.; Chen, B.; Wang, Y.; Yu, H.; Jiang, X.; Yang, J. Continuously tunable true-time delay lines based on a one-dimensional grating waveguide for beam steering in phased array antennas. *Appl. Opt.* **2018**, *57*, 4998–5003. [[CrossRef](#)]
97. Halir, R.; Bock, P.J.; Cheben, P.; Ortega-Monux, A.; Alonso-Ramos, C.; Schmid, J.; Lapointe, J.; Xu, D.; Wanguemert-Perez, J.; Molina-Fernandez, I.; et al. Waveguide sub-wavelength structures: A review of principles and applications. *Laser Photonics Rev.* **2015**, *9*, 25–49.
98. Takeuchi, Y. Instantaneous Frequency Measurement System. U.S. Patent 3,991,365; US Patent and Trademark Office, Washington, DC, USA, 1976.
99. Tsui, J. *Microwave Receivers with Electronic Warfare Applications*; Wiley: New York, NY, USA, 1986.
100. Elisra Electronic Systems Ltd Microwave Division. A digital instantaneous frequency measurement receiver. *Microwave J.* **2007**, *50*, 276.

101. Herselman, P.L.; Cilliers, J.E. A digital instantaneous frequency measurement technique using high-speed analogue-to-digital converters and field programmable gate arrays. *South. Afr. J. Sci.* **2006**, *102*, 345–348.
102. Liu, L.; Jiang, F.; Yan, S.; Min, S.; He, M.; Gao, D.; Dong, J. Photonic measurement of microwave frequency using a silicon microdisk resonator. *Opt. Commun.* **2015**, *335*, 266–270. [[CrossRef](#)]
103. Burla, M.; Wang, X.; Li, M.; Chrostowski, L.; Azana, J. Wideband dynamic microwave frequency identification system using a low-power ultracompact silicon photonic chip. *Nat. Commun.* **2016**, *7*, 13004. [[CrossRef](#)] [[PubMed](#)]
104. Pagani, M.; Morrison, B.; Zhang, Y.; Casas-Bedoya, A.; Aalto, T.; Harjanne, M.; Kapulainen, M.; Eggleton, B.J.; Marpaung, D. Low-error and broadband microwave frequency measurement in a silicon chip. *Optica* **2015**, *2*, 751–756. [[CrossRef](#)]
105. Long, Y.; Zhang, Y.; Zhang, X.; Xia, J.; Dong, J.; Wang, J. Linear and nonlinear microwave responses of a microwave photonic filter based on a photonic crystal microcavity. *J. Appl. Phys.* **2017**, *121*, 233102. [[CrossRef](#)]
106. Qiu, H.; Zhou, F.; Qie, J.; Yao, Y.; Hu, X.; Zhang, Y.; Xiao, X.; Yu, Y.; Dong, J.; Zhang, X. A Continuously tunable sub-gigahertz microwave photonic bandpass filter based on an ultra-high-Q silicon microring resonator. *J. Lightwave Technol.* **2018**, *36*, 4312–4318. [[CrossRef](#)]
107. Li, L.; Ting, Y.; Jian-Ji, D. Microwave photonic filter with a continuously tunable central frequency using an SOI high-Q microdisk resonator. *Chin. Phys. B* **2014**, *23*, 093201. [[CrossRef](#)]
108. Long, Y.; Wang, J. All-optical tuning of a nonlinear silicon microring assisted microwave photonic filter: Theory and experiment. *Opt. Express* **2015**, *23*, 17758–17771. [[CrossRef](#)] [[PubMed](#)]
109. Liu, L.; Yang, Y.; Li, Z.; Jin, X.; Mo, W.; Liu, X. Low power consumption and continuously tunable all-optical microwave filter based on an opto-mechanical microring resonator. *Opt. Express* **2017**, *25*, 960–971. [[CrossRef](#)]
110. Long, Y.; Xia, J.; Zhang, Y.; Dong, J.; Wang, J. Photonic crystal nanocavity assisted rejection ratio tunable notch microwave photonic filter. *Sci. Rep.* **2017**, *7*, 40223. [[CrossRef](#)] [[PubMed](#)]
111. Ehteshami, N.; Zhang, W.; Yao, J. Optically tunable single passband microwave photonic filter based on phase-modulation to intensity-modulation conversion in a silicon-on-insulator microring resonator. In Proceedings of the 2015 International Topical Meeting on Microwave Photonics (MWP), Paphos, Cyprus, 26–29 October 2015; pp. 1–4.
112. Yang, W.; Yi, X.; Song, S.; Chew, S.X.; Li, L.; Nguyen, L. Tunable single bandpass microwave photonic filter based on phase compensated silicon-on-insulator microring resonator. In Proceedings of the OptoElectronics and Communications Conference (OECC) held jointly with 2016 International Conference on Photonics in Switching (PS), Niigata, Japan, 3–7 July 2016; pp. 1–3.
113. Ciminelli, C.; Dell’Olio, F.; Brunetti, G.; Conteduca, D.; Armenise, M.N. New microwave photonic filter based on a ring resonator including a photonic crystal structure. In Proceedings of the 19th International Conference on Transparent Optical Networks (ICTON), Girona, Spain, 2–6 July 2017; pp. 1–4.
114. Song, S.; Chew, S.X.; Yi, X.; Nguyen, L.; Minasian, R.A. Tunable single passband microwave photonic filter based on integrated optical double notch filter. *J. Lightwave Technol.* **2018**, *39*, 4557–4564. [[CrossRef](#)]
115. Liu, X.; Yu, Y.; Tang, H.; Xu, L.; Dong, J.; Zhang, X. Silicon-on-insulator-based microwave photonic filter with narrowband and ultrahigh peak rejection. *Opt. Lett.* **2018**, *43*, 1359–1362. [[CrossRef](#)] [[PubMed](#)]
116. Liu, L.; He, M.; Dong, J. Compact continuously tunable microwave photonic filters based on cascaded silicon microring resonators. *Opt. Commun.* **2016**, *363*, 128–133. [[CrossRef](#)]
117. Zhao, H.; Zhang, L.; Zhao, Y.; Ding, J.; Yang, L. Microwave photonic filter based on multistage high-order microring resonators. In Proceedings of the 2016 IEEE 13th International Conference on Group IV Photonics (GFP), Shanghai, China, 24–26 August 2016; pp. 96–97.
118. Casas-Bedoya, A.; Morrison, B.; Pagani, M.; Marpaung, D.; Eggleton, B.J. Tunable narrowband microwave photonic filter created by stimulated Brillouin scattering from a silicon nanowire. *Opt. Lett.* **2015**, *40*, 4154–4157. [[CrossRef](#)]
119. Gay, M.; Bramerie, L.; Neto, L.A.; Le, S.D.; Simon, J.; Peucheret, C.; Han, Z.; Checoury, X.; Moille, G.; Bourderionnet, J.; et al. Silicon-on-insulator RF filter based on photonic crystal functions for channel equalization. *IEEE Photonics Technol. Lett.* **2016**, *28*, 2756–2759. [[CrossRef](#)]
120. Burla, M.; Bazargani, H.P.; St-Yves, J.; Shi, W.; Chrostowski, L.; Azana, J.; Azana, J. Widely tunable microwave photonics notch filter based on a waveguide Bragg grating on silicon. In Proceedings of the Photonics Conference (IPC), San Diego, CA, USA, 12–16 October 2014; pp. 208–209.

121. Fang, K.; Matheny, M.; Luan, X.; Painter, O. Integrated silicon optomechanical cavity-waveguide devices for coherent photonic-microwave signal processing. In Proceedings of the Integrated Photonics Research, Silicon and Nanophotonics, Boston, MA, USA, 27 June–1 July 2015.
122. Bourderionnet, J.; Moille, G.; Combrie, S.; De Rossi, A.; Checoury, X.; Han, Z.; Gay, M.; Bramerie, L.; Simon, J.-C.; Peucheret, C. Silicon-on-insulator photonic crystal multi-tap microwave photonics filter. In Proceedings of the IEEE Photonics Conference (IPC), Waikoloa, HI, USA, 2–6 October 2016; pp. 281–282.
123. Marpaung, D.; Aryanfar, I.; Casas-Bedoya, A.; Choudhary, A.; Jiang, H.; Morrison, B.; Pagani, M.; Shahnia, S.; Vu, K.; Choi, D.Y. On-chip stimulated Brillouin scattering for microwave photonic signal processing. In Proceedings of the Optical Fiber Communications Conference and Exhibition (OFC), Anaheim, CA, USA, 20–24 March 2016; pp. 1–3.
124. Bogaerts, W.; De Heyn, P.; Van Vaerenbergh, T.; De Vos, K.; Kumar Selvaraja, S.; Claes, T.; Dumon, P.; Bienstman, P.; Van Thourhout, D.; Baets, R. Silicon microring resonators. *Laser Photonics Rev.* **2012**, *6*, 47–73.
125. Zhang, W.; Yao, J. A silicon photonic integrated frequency-tunable microwave photonic bandpass filter. In Proceedings of the International Topical Meeting on Microwave Photonics (MWP), Beijing, China, 23–26 October 2017; pp. 1–4.
126. Marpaung, C.; Morrison, B.; Pant, R.; Roeloffzen, C.; Leinse, A.; Hoekman, M.; Heideman, R.; Eggleton, B.J. Si<sub>3</sub>N<sub>4</sub> ring resonator-based microwave photonic notch filter with an ultrahigh peak rejection. *Opt. Express* **2013**, *21*, 23286–23294. [[CrossRef](#)]
127. Song, S.; Chew, S.X.; Yi, X.; Nguyen, L.; Minasian, R. Tunable single passband microwave photonic filter using a cascaded pair of microring resonators. In Proceedings of the International Topical Meeting on Microwave Photonics (MWP), Beijing, China, 23–26 October 2017; pp. 1–4.
128. Madjar, A.; Berceci, T. Microwave generation by optical techniques—A review. In Proceedings of the 36th European Microwave Conference, Manchester, UK, 10–15 September 2006; pp. 1099–1102.
129. Weiner, A.M. Ultrafast optical pulse shaping: A tutorial review. *Opt. Commun.* **2011**, *284*, 3669–3692. [[CrossRef](#)]
130. M8195A 65 GSa/s Arbitrary Waveform Generator. Available online: <https://www.keysight.com/en/pd-2443793-pn-M8195A/65-gsa-s-arbitrary-waveform-generator?pm=PL&nid=-33319.1102215&cc=CA&lc=eng> (accessed on 10 August 2018).
131. McKinney, J.D.; Leaird, D.E.; Weiner, A.M. Millimeter-wave arbitrary waveform generation with a direct space-to-time pulse shaper. *Opt. Lett.* **2002**, *27*, 1345–1347. [[CrossRef](#)] [[PubMed](#)]
132. Chou, J.; Han, Y.; Jalali, B. Adaptive RF-photonic arbitrary waveform generator. *IEEE Photonics Technol. Lett.* **2003**, *15*, 581–583. [[CrossRef](#)]
133. Lin, I.S.; McKinney, J.D.; Weiner, A.M. Photonic synthesis of broadband microwave arbitrary waveforms applicable to ultra-wideband communication. *IEEE Microw. Wirel. Compon. Lett.* **2005**, *15*, 226–228. [[CrossRef](#)]
134. Yao, J. Microwave photonics: Arbitrary waveform generation. *Nat. Photonics* **2010**, *4*, 79. [[CrossRef](#)]
135. Wang, J.; Shen, H.; Fan, L.; Wu, R.; Niu, B.; Varghese, L.T.; Xuan, Y.; Leaird, D.E.; Wang, X.; Gan, F.; et al. Reconfigurable radio-frequency arbitrary waveforms synthesized in a silicon photonic chip. *Nat. Commun.* **2015**, *6*, 5957. [[CrossRef](#)]
136. Zhang, W.; Yao, J. Silicon-based on-chip electrically-tunable spectral shaper for continuously tunable linearly chirped microwave waveform generation. *J. Lightwave Technol.* **2016**, *34*, 4664–4672. [[CrossRef](#)]
137. Zhang, W.; Yao, J. Photonic generation of linearly chirped microwave waveform with a large time-bandwidth product using a silicon-based on-chip spectral shaper. In Proceedings of the International Topical Meeting on Microwave Photonics (MWP), Paphos, Cyprus, 26–29 October 2015; pp. 1–4.
138. Chen, L.R.; Moslemi, P.; Wang, Z.; Ma, M.; Adams, R. Integrated microwave photonics for spectral analysis, waveform generation, and filtering. *IEEE Photonics Technol. Lett.* **2018**, *30*, 1838–1841. [[CrossRef](#)]
139. Yao, J. Photonic generation of microwave arbitrary waveforms. *Opt. Commun.* **2011**, *284*, 3723–3736. [[CrossRef](#)]
140. Zhang, W.; Zhang, J.; Yao, J. Largely chirped microwave waveform generation using a silicon-based on-chip optical spectral shaper. In Proceedings of the International Topical Meeting on Microwave Photonics (MWP), Sendai, Japan, 20–23 October 2014; pp. 51–53.
141. Spasojevic, M.; Chen, L.R. Discretely tunable optical delay lines using serial and step-chirped sidewall Bragg gratings in SOI. *Electron. Lett.* **2013**, *49*, 1. [[CrossRef](#)]

142. Tan, D.T.H.; Ikeda, K.; Saperstein, R.; Slutsky, B.; Fainman, Y. Chip-scale dispersion engineering using chirped vertical gratings. *Opt. Lett.* **2008**, *33*, 3013–3015. [[CrossRef](#)] [[PubMed](#)]
143. Notomi, M.; Yamada, K.; Shinya, A.; Takahashi, J.; Takahashi, C.; Yokohama, I. Extremely large group-velocity dispersion of line-defect waveguides in photonic crystal slabs. *Phys. Rev. Lett.* **2001**, *87*, 253902. [[CrossRef](#)] [[PubMed](#)]
144. Shao, H.; Yu, H.; Li, X.; Li, Y.; Jiang, J.; Wei, H.; Wang, G.; Dai, T.; Chen, Q.; Yang, J.; et al. On-chip microwave signal generation based on a silicon microring modulator. *Opt. Lett.* **2015**, *40*, 3360–3363. [[CrossRef](#)] [[PubMed](#)]
145. Zhang, W.; Yao, J. A silicon photonic integrated frequency-tunable optoelectronic oscillator. In Proceedings of the International Topical Meeting on Microwave Photonics (MWP), Beijing, China, 23–26 October 2017; pp. 1–4.
146. Zhang, W.; Yao, J. Silicon photonic integrated optoelectronic oscillator for frequency-tunable microwave generation. *J. Lightwave Technol.* **2018**, *36*, 4655–4663. [[CrossRef](#)]



© 2019 by the authors. Licensee MDPI, Basel, Switzerland. This article is an open access article distributed under the terms and conditions of the Creative Commons Attribution (CC BY) license (<http://creativecommons.org/licenses/by/4.0/>).